



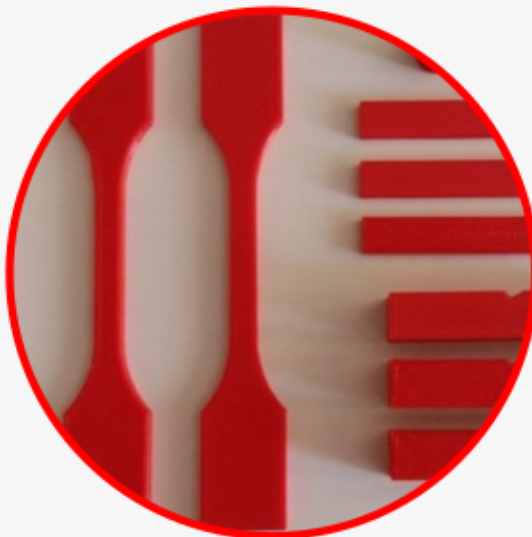
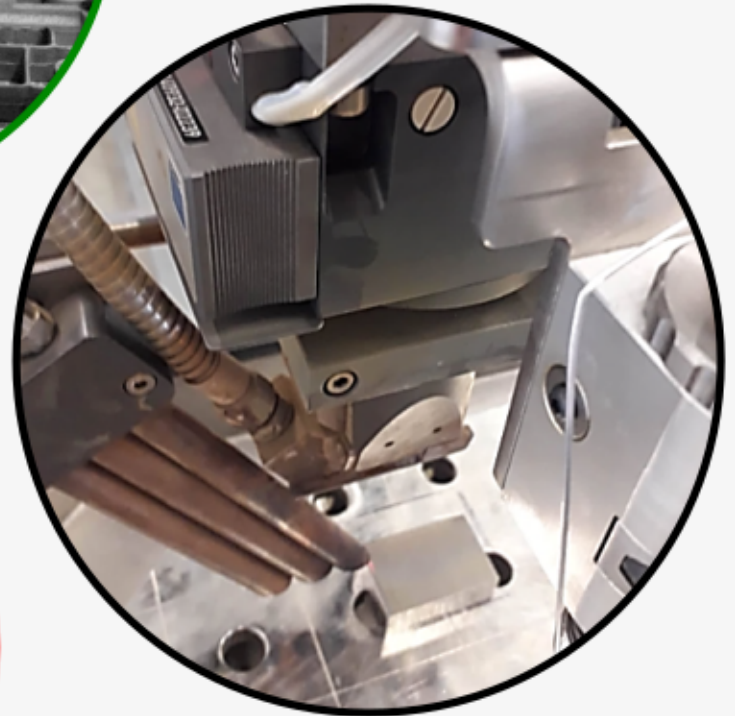
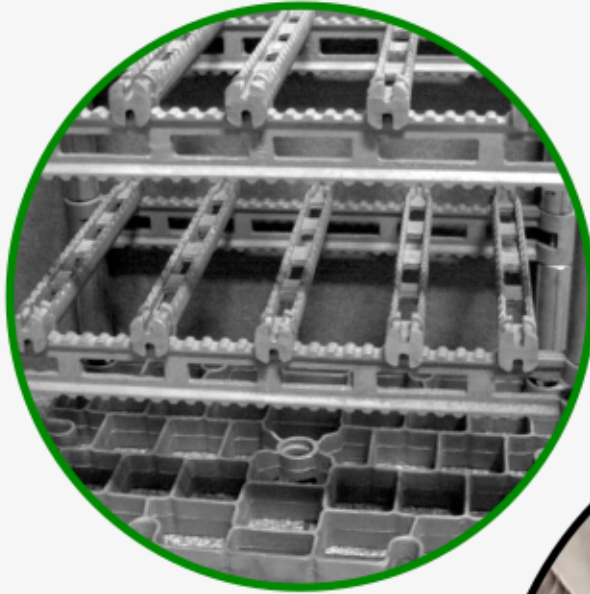
**AGH**

AGH UNIVERSITY OF SCIENCE AND TECHNOLOGY  
FACULTY OF FOUNDRY ENGINEERING

ISSN 2543-9901

# JOURNAL OF CASTING & MATERIALS ENGINEERING

QUARTERLY  
Vol. 4 No. 1/2020



# JCME



AGH UNIVERSITY OF SCIENCE AND TECHNOLOGY PRESS KRAKOW 2020

Editor-in-Chief of AGH University of Science and Technology Press  
*Jan Sas*

**Editorial Board of *Journal of Casting & Materials Engineering*:**

Editor-in-Chief

*Beata Grabowska, AGH University of Science and Technology, Poland*

Vice-Editor in Chief

*Marcin Górny, AGH University of Science and Technology, Poland*

Associate Editor

*Franco Bonollo, University of Padova, Italy*

Co-editors

*Marcin Brzeziński, AGH University of Science and Technology, Poland*

*Jarosław Jakubski, AGH University of Science and Technology, Poland*

*Artur Bobrowski, AGH University of Science and Technology, Poland*

*Karolina Kaczmarek, AGH University of Science and Technology, Poland*

Language Editor

*Aeddán Shaw*

Technical Editor

*Agnieszka Rusinek*

Cover Designer

*Małgorzata Biel*

*The articles published in the Journal of Casting & Materials Engineering have been given a favorable opinion by the reviewers designated by the Editorial Board.*

**www:**

<https://journals.agh.edu.pl/jcme/>

© Wydawnictwa AGH, Krakow 2020



AGH UNIVERSITY OF SCIENCE AND TECHNOLOGY PRESS    KRAKOW 2020

Wydawnictwa AGH (AGH University of Science and Technology Press)

al. A. Mickiewicza 30, 30-059 Kraków

tel. 12 617 32 28, 12 638 40 38

e-mail: [redakcja@wydawnictwoagh.pl](mailto:redakcja@wydawnictwoagh.pl)

<http://www.wydawnictwa.agh.edu.pl>

# Contents

**Stefan Szczepanik, Piotr Nikiel**

Influence of Structural Characteristics on the Mechanical Properties of  
FDM Printed PLA Material 1

**Andrzej Trytek, Mirosław Tupaj, Ján Majerník, Štefan Gašpár,**

**Wiktoria Zbyrad-Kołodziej, Karol Łysiak**  
Surface Remelting of Mold Inserts Made of NC11 Steel 9

**Andrzej Drotlew, Bogdan Piekarski**

Connecting Castings for Operation  
under Conditions of Cyclic Temperature Changes 16

# Influence of Structural Characteristics on the Mechanical Properties of FDM Printed PLA Material

Stefan Szczepanik<sup>\*</sup> , Piotr Nikiel 

AGH University of Science and Technology, Faculty of Metals Engineering and Industrial Computer Science,  
Mickiewicza 30 Ave., 30059 Krakow, Poland  
*\*e-mail: [szczepan@metal.agh.edu.pl](mailto:szczepan@metal.agh.edu.pl)*

© 2020 Authors. This is an open access publication, which can be used, distributed and reproduced in any medium according to the Creative Commons CC-BY 4.0 License requiring that the original work has been properly cited.

Received: 11 November 2019/Accepted: 29 January 2020/ Published online: 30 March 2020  
This article is published with open access at AGH University of Science and Technology Press

---

## Abstract

The present study reports on the influence of printing process parameters, architecture, raster, infill orientation and filling on the density, macrostructure, and mechanical properties, including impact resistance, of biodegradable polymer parts fabricated in polylactide (PLA) on a desktop printer. It complements and considers phenomenologically the results of recently published similar studies, including the use of recycled filament. In our study, complex mechanical properties for the samples printed at the same time on a Replicator 2 printer were investigated. Three samples were printed for each test. Full mechanical characteristics (tensile, compression and bend strengths and impact resistance) of the printed PLA material are reported. This is the novelty in comparison to other studies, where the samples test were printed individually or in a series for each test. The shape and thickness of the layered macrostructure, the presence of holes inside the layers, the number of shell perimeters and the fill density all influenced the tensile properties of the printed materials. These results show the possibility of printing with a 0.3, i.e. shorter printing time than 0.1, 0.15 and 0.18 mm layer thicknesses also reported, without significant decrease in mechanical properties. It is interesting to note that the compressive strengths, the yield of 70–80 MPa and a UTS 113–120 MPa for the printed material with a fill density of 94–96% are comparable with those of aluminum.

## Keywords:

additive manufacturing, polymer and plastics, polylactide, mechanical properties

---

## 1. INTRODUCTION

The relation between mechanical properties and process parameters (gap, raster width and angle) for polycarbonate parts produced by Stratasys FDM Fused Deposition Modeling (FDM) Technology has been considered e.g. by Masood [1] and Masood et al. [2] and the results compared with moulded and extruded parts. Bellini and Güçeri [3] investigated the mechanical properties of acrylonitrile butadiene styrene (ABS) parts fabricated by FDM and proposed how building direction and path determine the mechanical properties. Novakova-Marcincinova and Novak-Marcincin [4] tensile tested ABS material produced with different geometric parameters by FDM rapid prototyping technology. Smith and Dean's [5] study focused on the determination of tensile strength, yield strength and modulus of elasticity for polycarbonate material produced by fused deposition modeling with different values of build orientation.

Identification of optimum values for the main geometric parameters of the FDM printing process to achieve minimum cost was investigated by Durgun and Ertan [6].

Several research teams [7–10] have investigated printing by the biodegradable polylactide (PLA) and reported on the resultant mechanical properties. Lanzotti et al. [7] reported the effect of process parameters on tensile properties, including a decrease in strength as the infill orientation approaches 90 degrees and an increase as the perimeters increase. Grasso et al. [8] went on to show a strong correlation between stiffness and strength with infill orientation and temperature. They considered the deformed geometry of the filament approaching the glass transition region of the polymer according to the deposition orientation. Letcher and Waytashek [9] printed each specimen individually at the center of the printing bed and accordingly obtained less scatter in the properties investigated, including fatigue. Anderson [10] additionally considered the use of recycled

filament and concluded that, overall, the mechanical properties of 3D printed specimens from recycled PLA filament were similar to virgin properties, but the scatter was larger.

The present study reports on the influence of the printing process parameters, architecture, raster, infill orientation and filling on the density, macrostructure, and mechanical properties, including impact resistance, of printed PLA specimens and compares and contrasts the new results with those which have been published previously. Full mechanical characteristics, tensile, compression and bend strengths and impact resistance, of the printed PLA material are reported.

## 2. MATERIALS AND TESTING METHODS

The PLA Fiberlogy filament used for printing test specimens has the following tensile properties: tensile strength *UTS* 55.4 MPa and yield stress *YS* 45 MPa. Samples' design for tensile, compressive, bend and impact testing are illustrated in Figure 1 and their detailed characteristics in Table 1. Test samples were marked as follows: I – series, no., layer thickness [mm], fill volume [%], and architecture / structure. All samples were fabricated on a Replicator 2 printer from red PLA polymer at the CadXpert Company in Krakow.

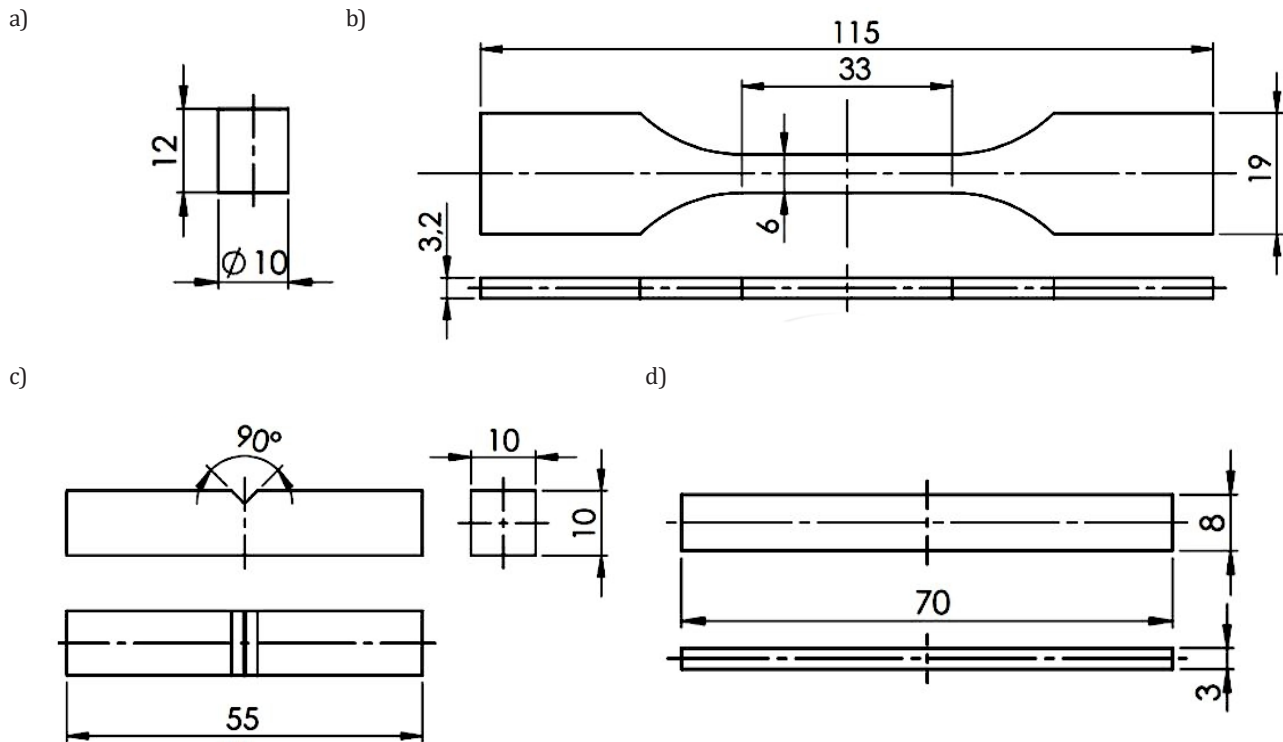


Fig. 1. Drawings of the test samples (all dimensions in millimeters)

**Table 1**  
Specifications of the samples: printed layer thickness, filling and specimen architecture


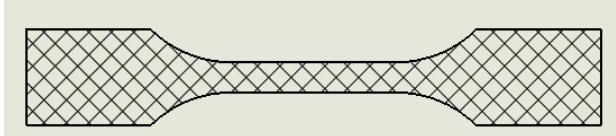
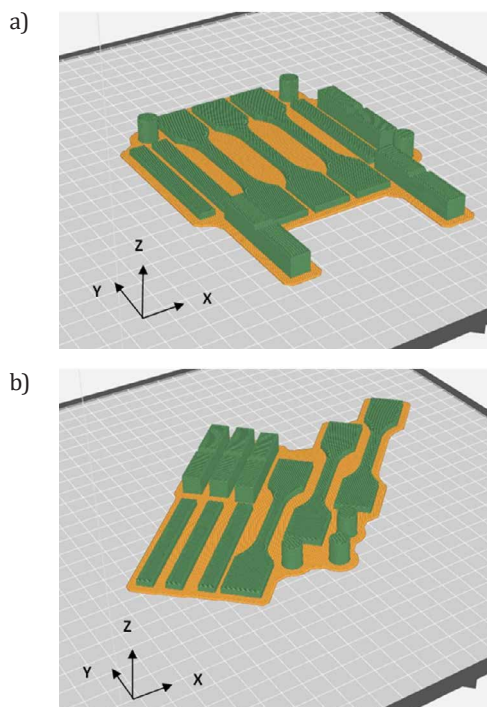
Series	No. of set samples	Layer thickness, mm	Filling, %	Architecture of filled material
I	1	0.1	50	
	2	0.3		
	3	0.1	100	
	4	0.3		
II	5	0.1	50	
	6	0.3		
	7	0.1	100	
	8	0.3		

Figure 2 shows the virtual arrangement for printing on the plate in the MakerBot Print program. The temperature of the printing nozzle was 215°C, the time and material consumption are recorded in Table 2.

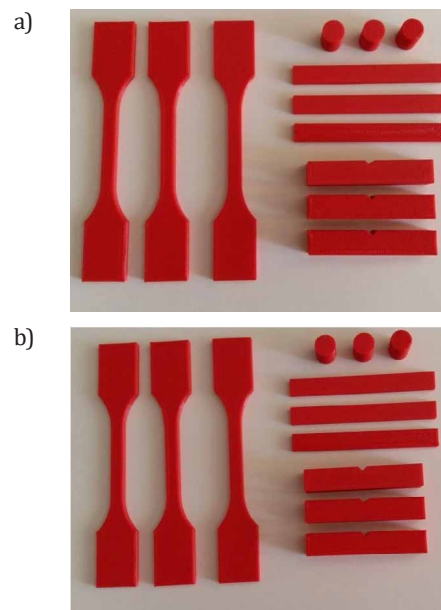
Three samples were fabricated for every specimen shape, with a total of 96. Figure 3 shows test samples printed for variant I. Mechanical properties: Young’s modulus, engineering yield (tensile and compressive) and ultimate tensile stress and elongation, were determined at room temperature on an Instron 4502 machine at a rate of 5 mm/minute. For three point bending, the span was 48 mm. Charpy impact resistance was determined for notched samples.



**Fig. 2.** Virtual arrangement for printing on the plate in the MakerBot Print program, the path of printing the sample with regard to the axis, raster orientation direction: a) 0° (series I); b) ±45°(series II)

**Table 2**  
Printing parameters

Series	No. of set samples	Layer thickness, mm	Filling, %	Printing time, h:min	Filament consumption, g
I	1	0.1	50	4.44	51
	2	0.3		2.55	
	3	0.1	100	5.33	66
	4	0.3		3.43	
II	5	0.1	50	5.39	53
	6	0.3		3.26	
	7	0.1	100	6.37	69
	8	0.3		4.23	

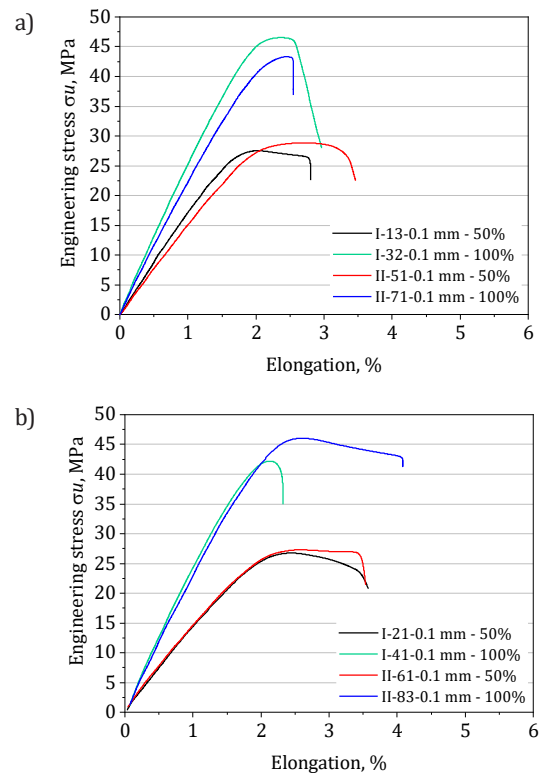


**Fig. 3.** Printed PLA samples: a) series I-1, raster orientation direction 0°; b) series II-1, raster orientation direction 45°

### 3. RESULTS

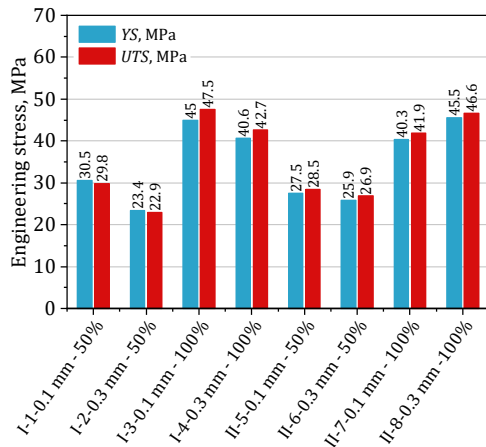
#### 3.1. Tensile testing

Figure 4 presents nominal stress-nominal strain curves for different type of specimens.

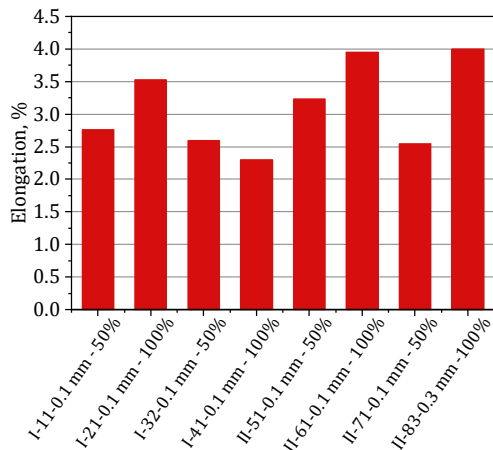


**Fig. 4.** Engineering stress-strain plots for 50% and 100% filling: a) 0.1 mm; b) 0.3 mm layer thickness (samples were marked follows: series, no. of set samples, no. of sample, layer thickness, filling, see Table 1)

Cracking of samples took place perpendicularly to the tensile axis after small elongations. Figure 5 collects the average values of yield and tensile strengths and Figure 6 total elongation. Error bar analysis is presented in the "Discussion" section (see. Tab. 3).



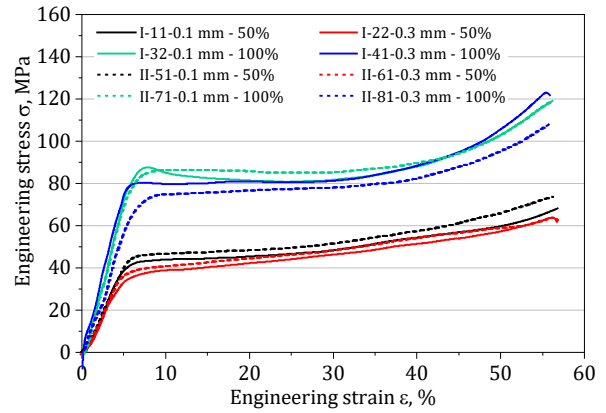
**Fig. 5.** Average values of yield and ultimate tensile stresses of the printed material (samples were marked: series, no. of set samples, layer thickness, filling, see Table 1)



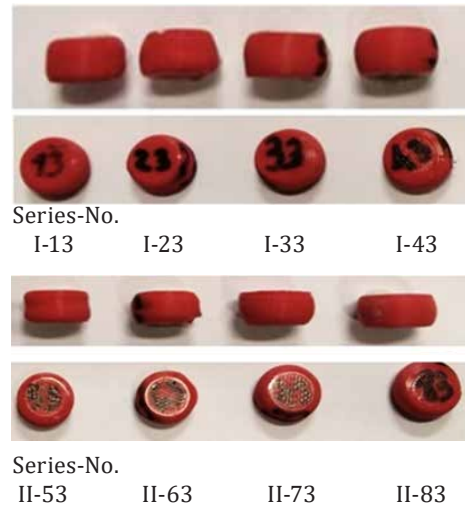
**Fig. 6.** Values of total tensile elongation of selected printed samples (samples were marked: series, no. sample, layer thickness, filling, see Table 1)

### 3.2. Compression testing

Figure 7 illustrates engineering compressive stress-strain plots and Figure 8 shows the samples after compression.



**Fig. 7.** Plot of engineering compressive stress-strain (samples were marked follows: series, no. of set samples, no. of sample, layer thickness, filling, see Table 1)



**Fig. 8.** Specimens after compression testing (samples were marked: series, no. samples (see Table 1)

**Table 3**  
Mechanical properties of printed PLA materials

No.	Layer thickness, mm	Architecture /filling	Mechanical properties							Impact resistance, J/cm <sup>2</sup>
			tensile			compression		bend		
			$E$ , GPa	$YS_{0.2}$ , MPa	$UTS$ , MPa	$YC_{0.2}$ , MPa	$CS$ , MPa	$\sigma_{b0.2}$ , MPa	$\sigma_b$ , MPa	
1	0.1		1.6 ± 0.17	31 ± 3	30 ± 2	41 ± 2	70 ± 2	67 ± 3	68 ± 3	0.37 ± 0.03
2	0.3	/50%	1.4 ± 0.06	23 ± 3	23 ± 4	33 ± 1	66 ± 1	53 ± 5	55 ± 2	0.33 ± 0.03
3	0.1		2.5 ± 0.04	45 ± 4	48 ± 1	84 ± 1	121 ± 3	99 ± 1	102 ± 1	0.45 ± 0.03
4	0.3	/100%	2.3 ± 0.13	41 ± 1	43 ± 1	76 ± 1	121 ± 3	82 ± 1	85 ± 2	0.42 ± 0.03
5	0.1		1.5 ± 0.06	28 ± 2	29 ± 2	41 ± 1	73 ± 3	61 ± 3	63 ± 4	0.28 ± 0.07
6	0.3	/50%	1.4 ± 0.09	26 ± 1	27 ± 1	35 ± 3	62 ± 10	60 ± 1	65 ± 1	0.33 ± 0.04
7	0.1		2.1 ± 0.19	40 ± 1	42 ± 2	80 ± 2	113 ± 3	70 ± 3	77 ± 1	0.42 ± 0.05
8	0.3	/100%	2.2 ± 0.06	46 ± 2	47 ± 2	71 ± 4	113 ± 3	99 ± 1	101 ± 4	0.38 ± 0.04

$E$  – Young's modulus,  $YS_{0.2}$  – yield stress,  $UTS$  – ultimate tensile stress,  $YC_{0.2}$  – yield stress in compression,  $CS$  – ultimate compression stress,  $\sigma_{b0.2}$  – yield stress in bending,  $\sigma_b$  – max nominal stress in bending

Mean strength values of compression yield strength  $YS_{0.2}$  and compression strength  $CS$  are shown in Figure 9.

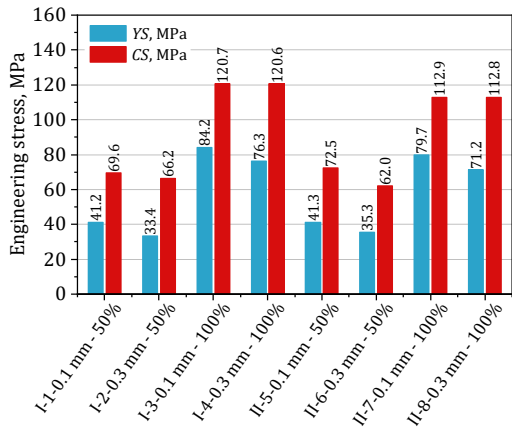


Fig. 9. Average compressive yield stress values  $YS_{0.2}$  and compression strength  $CS$ , for printed thicknesses 0.1 or 0.3 mm and filling 50 or 100% (legend: series, no. of set samples, layer thickness [mm], filling, architecture, see Figure 1)

### 3.3. Bend testing

Figure 10 shows plots of bending stress versus ram displacement, and Figure 11 summarizes the yield and (nominal) bend strength data. Fractographs are shown in Figure 12. Holes between layers and filament changes are visible on the fracture surfaces of the printed samples.

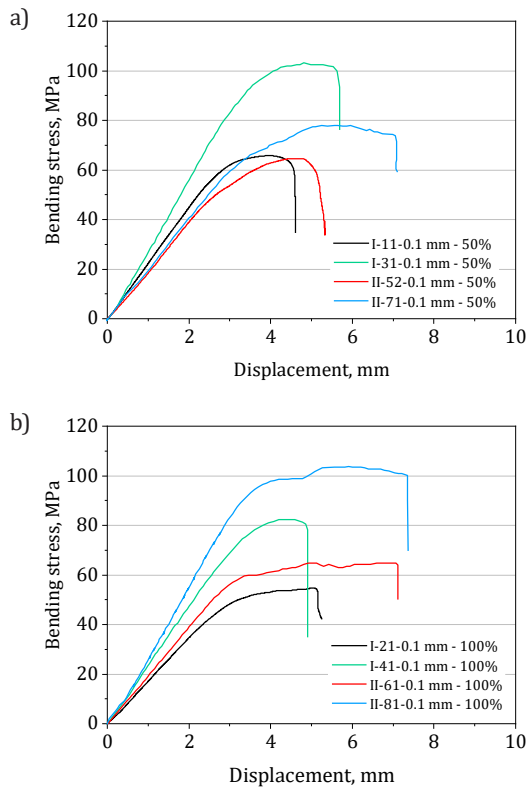


Fig. 10. Plots of bending stress vs ram displacement (samples were marked: series, no. of set samples, layer thickness, filling, see Table 1)

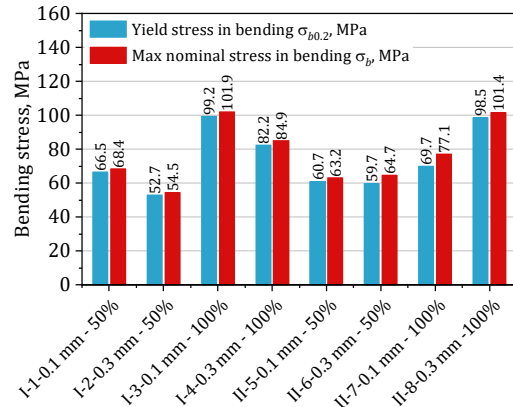


Fig. 11. Average values of the yield stress  $\sigma_{b0.2}$  and nominal bend strength  $\sigma_b$  at failure (legend: series, no. of set samples, layer thickness, filling, see Table 1)

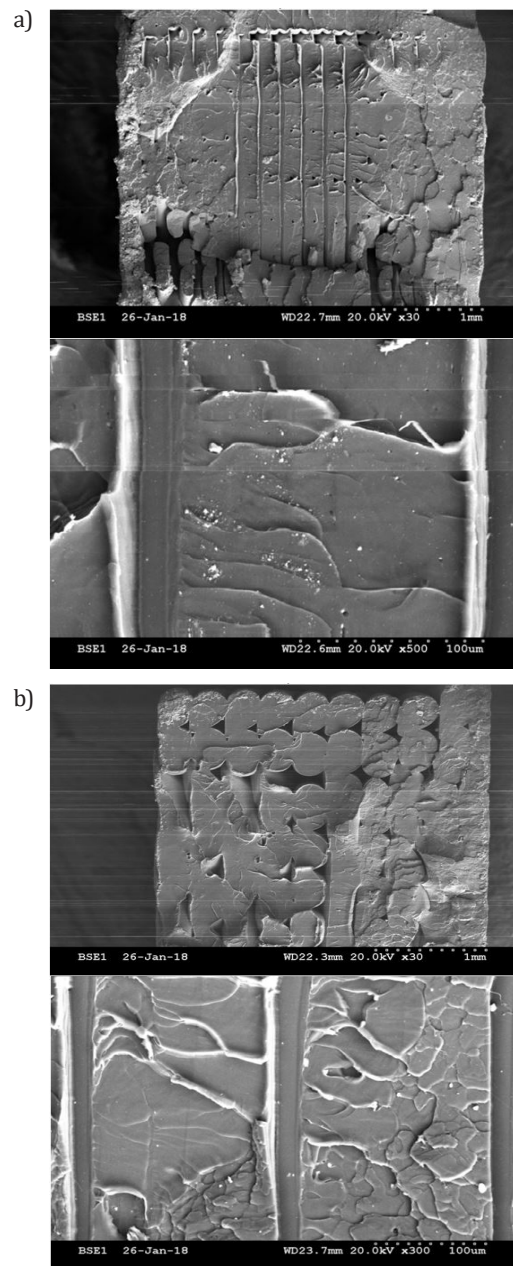
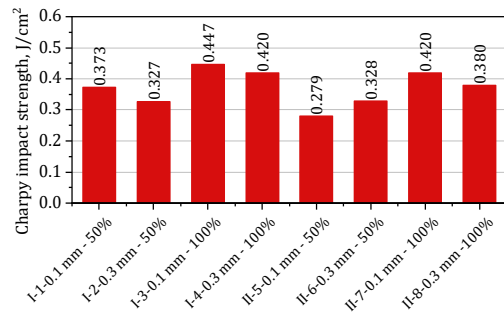


Fig. 12. Fracture surfaces (SEM) of specimens after bending, layer thickness: a) 0.1 mm and filling 100%; b) 0.3 mm and filling 100%

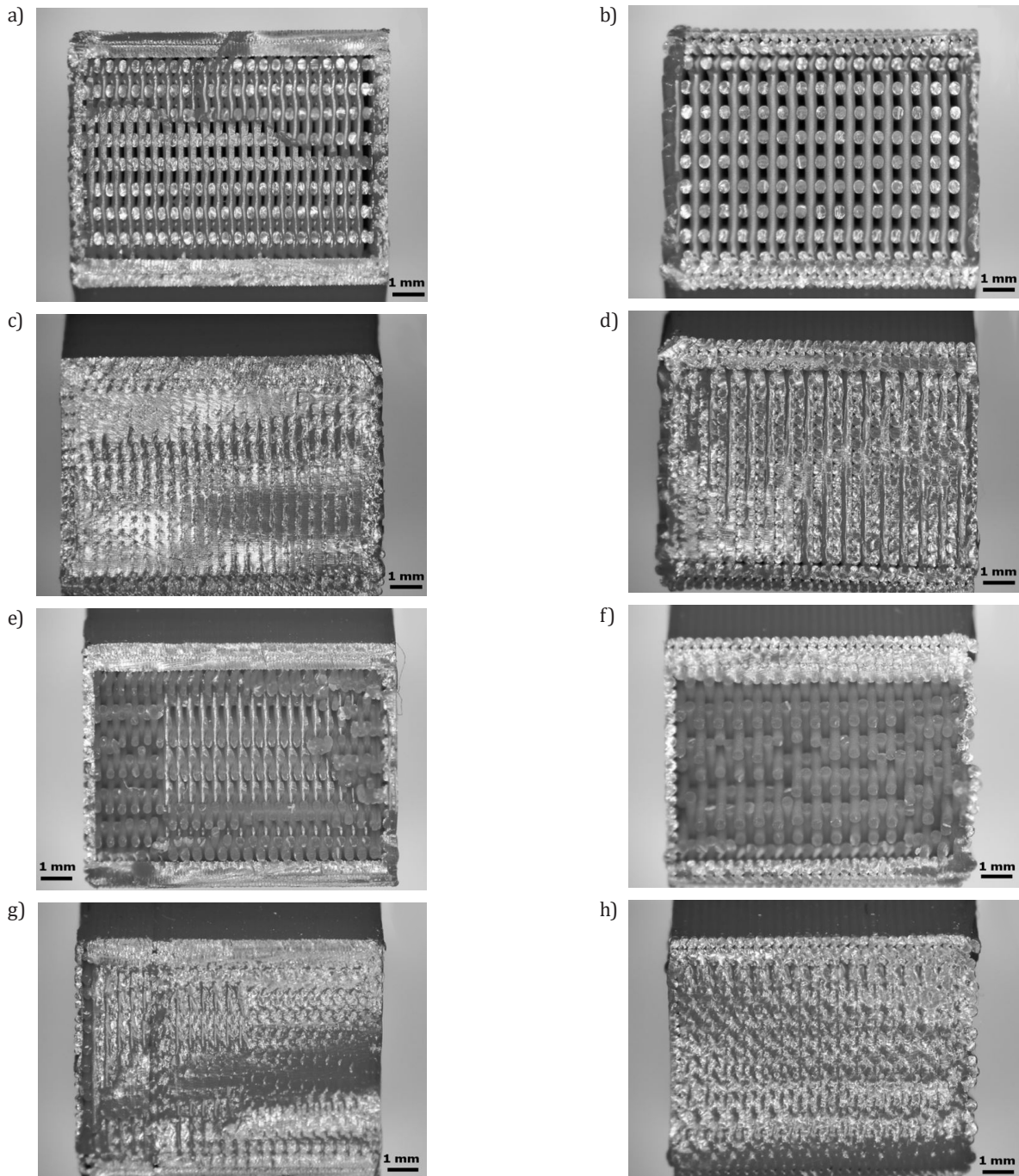


### 3.4. Impact resistance testing

The results of the Charpy test are shown in Figure 13. Impact resistance depends on the path of printing; higher values were recorded for material printed with a parallel path to the axis (series I) than with  $\pm 45^\circ$  path angles (series II). Holes are observed on fracture surfaces of Charpy specimens (Fig. 14) between filaments and layers. More holes and weaker joining are observed for printed material with 50% filling ratio (Figs. 14 a, b and Figs. 14 e, f). Better joining of the filaments and layers took place in samples with a path  $\pm 45^\circ$  and  $0^\circ$  and a 100% filling.



**Fig. 13.** Average impact resistance, for printed thicknesses 0.1 or 0.3 mm and filling 50 or 100% (legend: series, no. of set samples, layer thickness, filling, see Table 1)



**Fig. 14.** Fracture surfaces of specimens after Charpy testing: a) I-1; b) I-2; c) I-3; d) I-4; e) II-5; f) II-6; g) II-7; h) II-8 (legend see Table 1)

#### 4. DISCUSSION

The density of printed materials depends on layer thickness, filling and architecture established by the printing temperature. To be noted are differences in printing, e.g. layer thickness and number of shell perimeters. The mean densities of printed samples were: series I-1 – 0.82, I-2 – 0.79, I-3 – 1.23, I-4 – 1.19 and series II-5 – 0.82, II-6 – 0.01, II-7 – 1.19, II-8 – 1.18 g/cm<sup>3</sup>, i.e. smaller than the 1.24 g/cm<sup>3</sup> density of PLA filament produced by injection moulding. The relative density was in the range 0.63–0.65 for 50% and 0.94–0.98 for 100% filling. Fill density strongly influenced all the mechanical properties of the printed materials. The layer thickness and architecture have a smaller influence than filling by established printing parameters. Holes are a further factor influencing mechanical properties. The layered macrostructure, including holes, is shown in Figure 12 and in Figure 14 on the fractographs of bend specimens. Impact resistance of our printed PLA is comparable to that of moulded material 1.3–5.5 KJ/m<sup>2</sup> [11].

Table 3 summarizes the mechanical properties of printed PLA, i.e. mean value and confidence interval with  $\alpha = 0.05$  for the 3 elements population. More repeatable values of Young's modulus were for materials with the relative density 0.94–0.98. Tensile stresses were about 40% higher for 100% filled printed material, comparable for material with a parallel and  $\pm 45^\circ$  printed structure. Elongation depended on layer thickness, filling and structure. For parallel printed structure, layer thickness 0.1 and fillings 50 and 100%, tensile elongation was  $\sim 2.8\%$  for both, and for layer thickness 0.3 it was 3.5% and 2.3%, respectively. For printed parallel material structure, it was 3.2% and 2.5%, and was higher 3.9% and 4.0% for material structure  $\pm 45^\circ$ .

All the strengths were, as is generally the case for polymers, in ascending order: compressive, flexural. The differences between tensile and compressive result from the nature of deformation mechanisms in polymers. For bend strength, there is the additional problem of the complex elastic-plastic stress distribution in a bending beam when the tensile and compressive yield stresses are unequal.

Only phenomenological correlations, e.g. with density and architecture, are presented. For additional aspects, the reader is referred to the discussions of Lanzotti et al. [7] and Grasso et al. [8], whose tensile results and those of Letcher and Waytashek [9], Anderson [10] and Ezech and Susmel [12] are presented in a Table 4. This summarizes the strength properties of printed PLA in comparison with strength properties reported in [7–12].

It is clearly discernible that, when direct comparison can be made, Young's moduli reported by Lanzotti et al. [7] and Grasso et al. [8] are somewhat higher than now reported. *UTS* are slightly higher, but the small influence of infill orientation (0/90 and  $\pm 45^\circ$ ) and layer thickness of 0.1–0.3 mm is to be noted. Yield stress reported by Anderson [10] is comparable at 40 MPa for layer thickness 0.4 mm. *UTS* reported by Letcher and Waytashek [9], 58 and 64 MPa for infill orientation 0 and  $\pm 45^\circ$ , is higher than our values.

One interesting and perhaps fortuitous correlation relates to printed material with parallel infill and is connected with density and strength. For MIM, the PLA filament has 55 MPa tensile strength and a yield strength of 45 MPa. Using the same scaling factor for density and strength, for 0.66 relative density, tensile and yield strengths evaluate to 36 MPa and 30 MPa respectively, and the measured values were 30 MPa and 29 MPa. For 0.96 relative density evaluated strength and yield stresses of 53 MPa and 43 MPa are to be compared with experimental values of 47 MPa and 45 MPa.

**Table 4**  
Average tensile properties at room temperature

Results source	Property				Parameters		
	<i>E</i> , GPa	<i>UTS</i> , MPa	<i>YS</i> , MPa	$\sigma_b$ , MPa	fill density, %	infill orientation	layer thickness, mm
Lanzotti [7]	3.4	49	–	–	100*	0/90	0.2
	3.0	48	–	–		$\pm 45$	0.15
Grasso [8]	2.2	45	–	–	–	0/90	0.18
	2.8	50	–	–	–	$\pm 45$	–
Letcher and Waytashek [9]	3.33	58	–	–	100*	0	–
	3.49	64	–	–		$\pm 45$	–
Anderson [10]	4.26	–	40	–	–	–	0.4
Ahmed and Susmel [12]	1.16	16	14	–	60	0	0.1
	2.06	26	24	–	90	0	0.1
Current	1.6	30	23	68	63	0/90	0.1
	1.4	23	23	54	64	0/90	0.3
	2.5	47	45	102	94	0/90	0.1
	2.3	43	41	85	94	0/90	0.3
	1.5	28	27	63	65	$\pm 45$	0.1
	1.4	27	26	65	65	$\pm 45$	0.3
	2.2	42	40	77	98	$\pm 45$	0.1
	2.2	47	45	101	98	$\pm 45$	0.3

\* printer parameter, not calculated for the sample

## 5. CONCLUSIONS

Full mechanical characteristics (tensile, compression and bend strengths and impact resistance) of the printed PLA material are reported. The layered structure resulting from the filament polymer source and holes inside the layers produce material with an irregularly shaped macrostructure which influences its properties. The macrostructure changes probably occur as a result of the thermal influence on the starting polymer filament. These results shown possibility printing with a 0.3, i.e. shorter printing time than 0.1 mm, 0.15 mm and 0.18 mm layer thicknesses also reported, without significant decrease in mechanical properties.

These results are comparable to those previously reported and show that reasonably good and reproducible mechanical properties are achievable with desktop [entry level] printers. It is interesting to note that the compressive strengths, the yield of 70–80 MPa and a UTS 113–120 MPa for the printed material with a fill density of 94–96% are comparable with those of aluminum.

## Acknowledgements

*The research was financed by the Ministry of Science and Higher Education (AGH - research subsidy no. 16.16.110.663, task 3).*

## REFERENCES

- [1] Masood S.H. (2014). *Advances in fused deposition modelling*. In: Hashmi S., Batalha G.F., Van Tyne C.J. & B. Yilbas (Eds.), *Comprehensive Materials Processing*. Elsevier.
- [2] Masood S.H., Mau K. & Song W.Q. (2010). Tensile properties of processed FDM polycarbonate material. *Materials Science Forum*, 654/656(1), 2556–2559, <https://doi.org/10.4028/www.scientific.net/MSF.654-656.2556>
- [3] A. Bellini & Güçeri S. (2003). Mechanical characterization of parts fabricated using fused deposition modeling. *Rapid Prototyping Journal*, 9(4), 252–264.
- [4] Novakova-Marcincinova L. & Novak-Marcincin J. (2014). Testing ABS material tensile strength for fused deposition modeling rapid prototyping method. *Advanced Materials Research*, 912/914(1), 370–373, <https://doi.org/10.4028/www.scientific.net/AMR.912-914.370>
- [5] Smiths W.C. & Dean R.W. (2013). Structural characteristics of fused deposition modeling polycarbonate material. *Polymer Testing*, 32(8), 1306–1312, <https://doi.org/10.1016/j.polymertesting.2013.07.014>
- [6] Durgun I. & Ertan R. (2014). Experimental investigation of FDM process for improvement of mechanical properties and production cost. *Rapid Prototyping Journal*, 20(3), 228–235, <http://dx.doi.org/10.1108/RPJ-10-2012-0091>
- [7] Lanzotti A., Grasso M., Staiano G. & Martorelli M. (2015). The impact of process parameters on mechanical properties of parts fabricated in PLA with an open-source 3-D printer. *Rapid Prototyping Journal*, 21(5), 604–617, <https://doi.org/10.1108/RPJ-09-2014-0135>
- [8] Grasso M., Azzouz L., Ruiz-Hincapie P., Zarrelli M. & Ren G. (2018). Effect of temperature on the mechanical properties of 3D-printed PLA tensile specimens. *Rapid Prototyping Journal*, 24 (8), 1337–1346, <https://doi.org/10.1108/RPJ-04-2017-0055>
- [9] Letcher T. & Waytashek M. (2014). Material property testing on of 3D-printed specimen in PLA on entry-level 3D printer. *Proceedings of the ASME 2014 International Mechanical Engineering Congress and Exposition*. Volume 2A: Advanced Manufacturing. Montreal, November 14–20. ASME, <https://doi.org/10.1115/IMECE2014-39379>
- [10] Anderson I. (2007). Mechanical Properties of Specimens 3D Printed with Virgin and Recycled Polylactic Acid. *3D Printing and Additive Manufacturing*, 4(2), 110–114, <https://doi.org/10.1089/3dp.2016.0054>
- [11] Polylactic Acid (PLA) Typical Properties, <http://prode.me/uploads/news/9a8c705752ed9f3279f0167013f574b0.pdf> [accessed 26.04.2019].
- [12] Ezeh O.H. & Susmel L. (2019). Fatigue strength of additively manufactured polylactide (PLA): effect of raster angle and non-zero mean stresses. *International Journal of Fatigue*, 42(4), 883–904, <https://doi.org/10.1111/ffe.12958>

# Surface Remelting of Mold Inserts Made of NC11 Steel

Andrzej Trytek<sup>a\*</sup>, Mirosław Tupaj<sup>a</sup>, Ján Majerník<sup>b</sup>, Štefan Gašpár<sup>c</sup>,  
Wiktor Zbyrad-Kołodziej<sup>a</sup>, Karol Łysiak<sup>a</sup>

<sup>a</sup> Rzeszów University of Technology, The Faculty of Mechanics and Technology, Stalowa Wola 37-450, E. Kwiatkowskiego 4, Poland

<sup>b</sup> The Department of Mechanical Engineering, Faculty of Technology Institute of Technology and Business in České Budějovice, Okružní 517/10, 370 01 České Budějovice, Czech Republic

<sup>c</sup> Faculty of Manufacturing Technologies of the Technical University of Kosice with a seat in Prešov, Bayerova 1, 080 01 Prešov, Slovak Republic

\*email: [trytek@prz.edu.pl](mailto:trytek@prz.edu.pl)

© 2020 Authors. This is an open access publication, which can be used, distributed and reproduced in any medium according to the Creative Commons CC-BY 4.0 License requiring that the original work has been properly cited.

Received: 27 November 2019/Accepted: 20 February 2020/ Published online: 30 March 2020

This article is published with open access at AGH University of Science and Technology Press

---

## Abstract

In the study presented in this paper, the effect of a concentrated heat stream on geometry, microstructure, and hardness of superficial remeltings on NC11 steel is examined. The material is used for disposable mold inserts exposed to intensive abrasive wear in the course of the press-molding of hard aggregate stampings for refractory bricks. As a result of local remelting, the hardness of the steel surface increased and its microstructure was altered. Macro- and microstructure of the remelted areas was examined with the use of optical microscopy and measurements of remelting area geometry were carried out for different parameters of the remelting process. Hardness measurements were taken in the remelting area and in the heat-affected zone. The state of stress in the material before remelting and in the remelted area was also evaluated.

## Keywords:

NC11 steel, mold inserts, concentrated heat stream, metallographic tests

---

## 1. INTRODUCTION

Bricks of refractory materials used to build foundry furnaces are molded from aggregates characterized by a high degree of hardness. In the course of the process of press-molding stampings for the bricks, aggregate grains rub against the metal mold surface which results in its wear. The wearing effect is intensified because of the sharpness of grain edges moved repeatedly in the course of the aggregate compacting process. The molds in which the stampings of refractory materials are formed are made of cold-work alloyed steels. To reduce the manufacturing cost and overhauling period, molds are given the form of a body with molding cavities which are lined with replaceable inserts. In view of the intensity of the wearing process, the lining elements should be characterized by a high resistance to abrasive wear. As a result of the excessive wear of mold inserts, stampings of refractory

material are prone to cracking and become unfit for the next production stage (firing). In view of stoppages and costs due to press retooling and replacement of the inserts, it became necessary to look for a solution enabling the extension of the service life of the components [1–8].

Extending the life of new machine parts is mainly by means of the use of new expensive materials and alloys and their heat treatment [9–13]. Repair of damage or the regeneration of parts of machinery worn as a result of operation usually involves supplementing the damaged area using powder spraying techniques or 3D printing [14–18]. The present authors' experience in the area of the local hardening of alloys with the use of a concentrated heat stream enabled them to advance the conclusion that, with the use of a laser beam, it would be possible to locally alter the microstructure of NC11 steel, increasing its hardness in comparison to the initial material, and thus extending the service life of the mold inserts [19–22].

## 2. THE RESEARCH

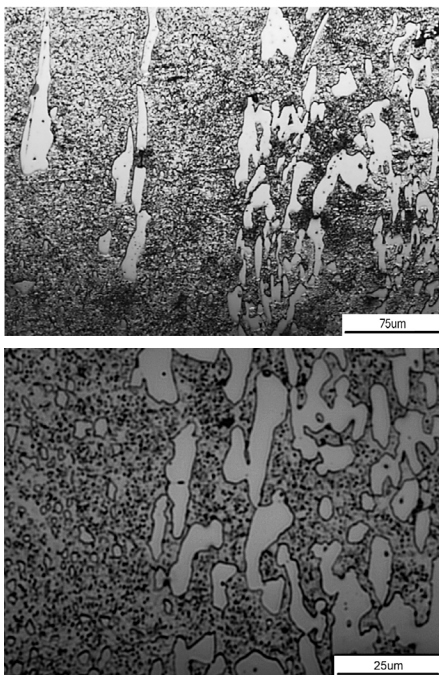
### 2.1. Research material

The tested material was NC11 steel containing about 12% Cr (Tab. 1). The material is a high-carbon cold-work steel designated as NC11, X210CrW12, 1.2436, X210Cr12, or 1.2080. NC11 steel is used to manufacture parts of machines and devices which are required to show high resistance to abrasive wear, e.g. drawing dies, blanking tools, threaders, cutting tools, forming dies, and punches [23].

NC11 steel is used to fabricate insert for cavities of moulds forming ceramic bricks of refractory materials. The microstructure of NC11 steel comprises a metal matrix with very fine carbides as well as long and thick carbide precipitates. The microstructure of NC11 steel carbides include chromium to the extent of 44% Cr and iron to 88% Fe, as well as manganese from about 0.15% to 0.29% Mn. The carbides differ in their shapes and lengths. The length of the carbides is from 2  $\mu\text{m}$ , and can be as long as 120  $\mu\text{m}$ . The structure of the matrix of NC11 includes 9% Cr, 87% Fe and 0.23% Mn [4]. The microstructure of the NC11 steel used for the purposes of the present study is shown in its initial state in Figure 1.

**Table 1**  
Chemical composition of NC11 steel [23]

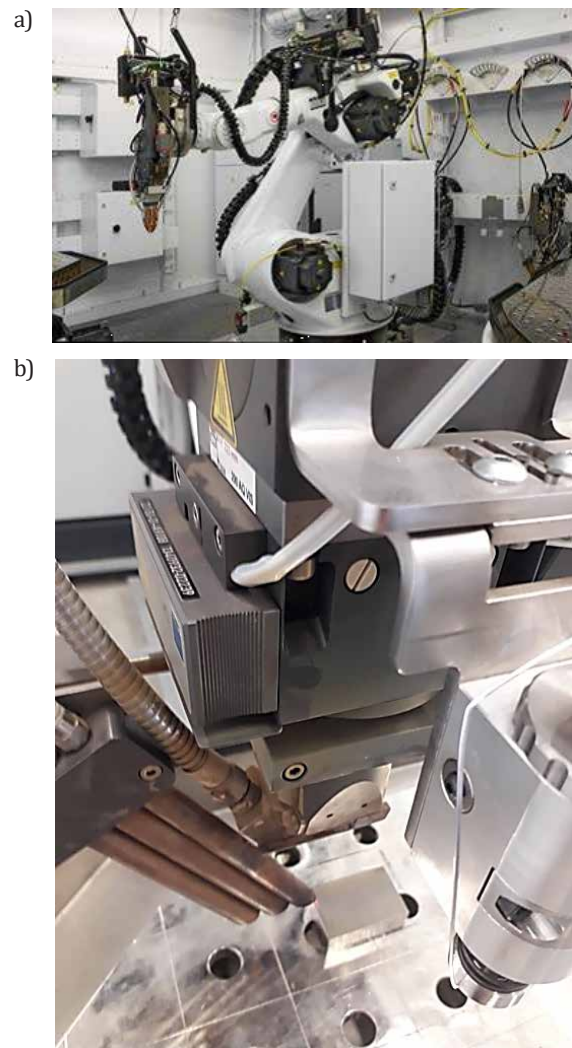
Element	C	Mn	Si	P	S
Content, % wt.	1.80–2.10	0.15–0.45	0.15–0.40	0.03 max.	0.03 max.
Element	Cr	Ni	Mo	W	V
Content, % wt.	11.0–13.0	0.35 max.	0.20 max.	0.20 max.	0.15 max.



**Fig. 1.** A view of the microstructure of NC11 steel; matrix and chromium carbides

### 2.2. The test setup

The setup for superficial remelting tests comprised an industrial booth equipped with a KUKA robot arm and a TruLaser ROBOT 5020 turnkey laser (TRUMPF) with the maximum power of 4 kW (diode laser with a wavelength of 1030 nm, beam diameter 0.9 mm). The setup is dedicated to developing and testing new technological processes as well as carrying out industrial operations such as welding, cutting, overlay welding, and heat treatment (Fig. 2). It is equipped with three independent heads intended for welding, cutting, and overlay welding (cladding).



**Fig. 2.** A view of the test stand for remelting with a TruLaser ROBOT 5020. The laser stand is equipped with a KUKA robot arm (a), replaceable heads for: welding (b), cutting and powder welding

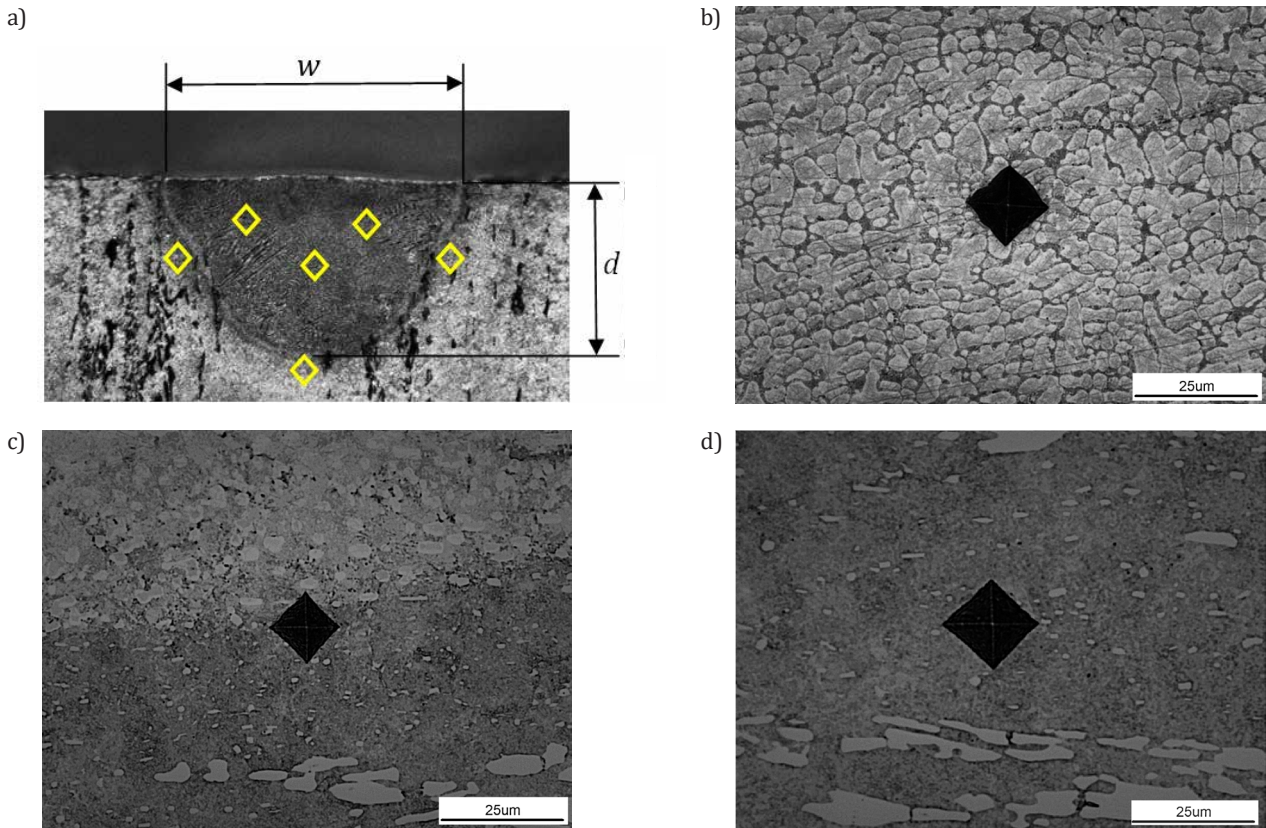
Due to the fact that a deep penetration of a small width is obtained with higher laser power, and these tests require surface hardening, low beam power was used. NC11 steel surface remelting tests were performed on specimens with dimensions 100 mm  $\times$  100 mm  $\times$  16 mm. Three remelting runs were realized at the same laser power  $P = 500$  W and at three different speeds of material surface scanning with a laser beam, namely 10 m/s, 20 m/s, and 30 m/s.

### 2.3. Research methodology

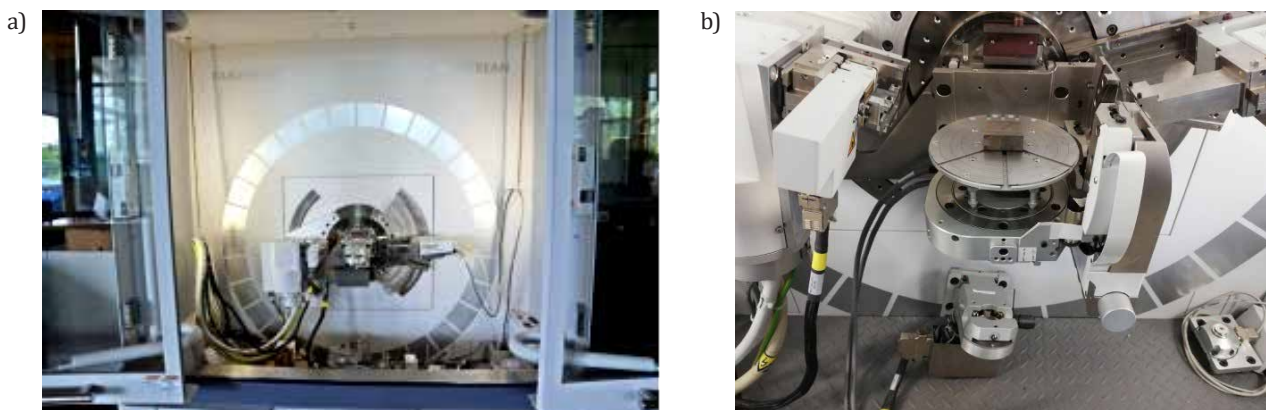
Examination of remelting areas on NC11 steel specimen surfaces consisted of macroscopic evaluation and measurements of remelting geometry. Moreover, metallographic examination was carried out, consisting of the observation of microstructures with the use of an optical microscope equipped with an advanced image analysis system, Multiscan v.08. Hardness measurements were taken with the use of a Nanovea nanoindentation microhardness tester. Figure 3 shows a schematic diagram according to which measurements of the remelting

geometry and material hardness in the remelting area and in the heat affected zone (HAZ) were taken.

To determine their state of stress, remelting areas were also examined with the use of an Empyrean X-ray diffractometer (Malvern Panalytical) as shown in Figure 4, equipped with a five-axis table and a copper X-ray tube. Parameters of the scan for the XRD residual stress measurement were the following: start position  $71.4890^{\circ}2\theta$ , end position  $76.4550^{\circ}2\theta$ , step size  $0.0260^{\circ}2\theta$ , scan step time 1196 seconds. For the purpose of stress analysis, HighScore Plus and X'Pert Stress software were used.



**Fig. 3.** Hardness measurements and melting geometry measurements: a) a schematic diagram ( $w$  – remelting width;  $d$  – remelting depth;  $\diamond$  – hardness measurement points); b) examples of hardness measurements in the area of melting; c) examples of hardness measurements in the HAZ; d) examples of hardness measurements in the initial material



**Fig. 4.** The stress analysis setup: a) Empyrean PANalytical diffractometer; b) diffractometer table with a specimen

## 2.4. Research results

Table 2 summarizes the results of the remelting geometry and hardness measurements taken in the remelting area and in HAZ and the values of stress determined in the remelting area, depending on the parameters of the process of surface remelting with laser.

The geometry of remelting areas formed on the NC11 steel specimen surface with a laser beam was different in each of the three tests. Both the width and depth of the remeltings decrease with the increase in the speed of scanning with the laser beam. The change in the melting geometry is primarily due to the amount of heat absorbed

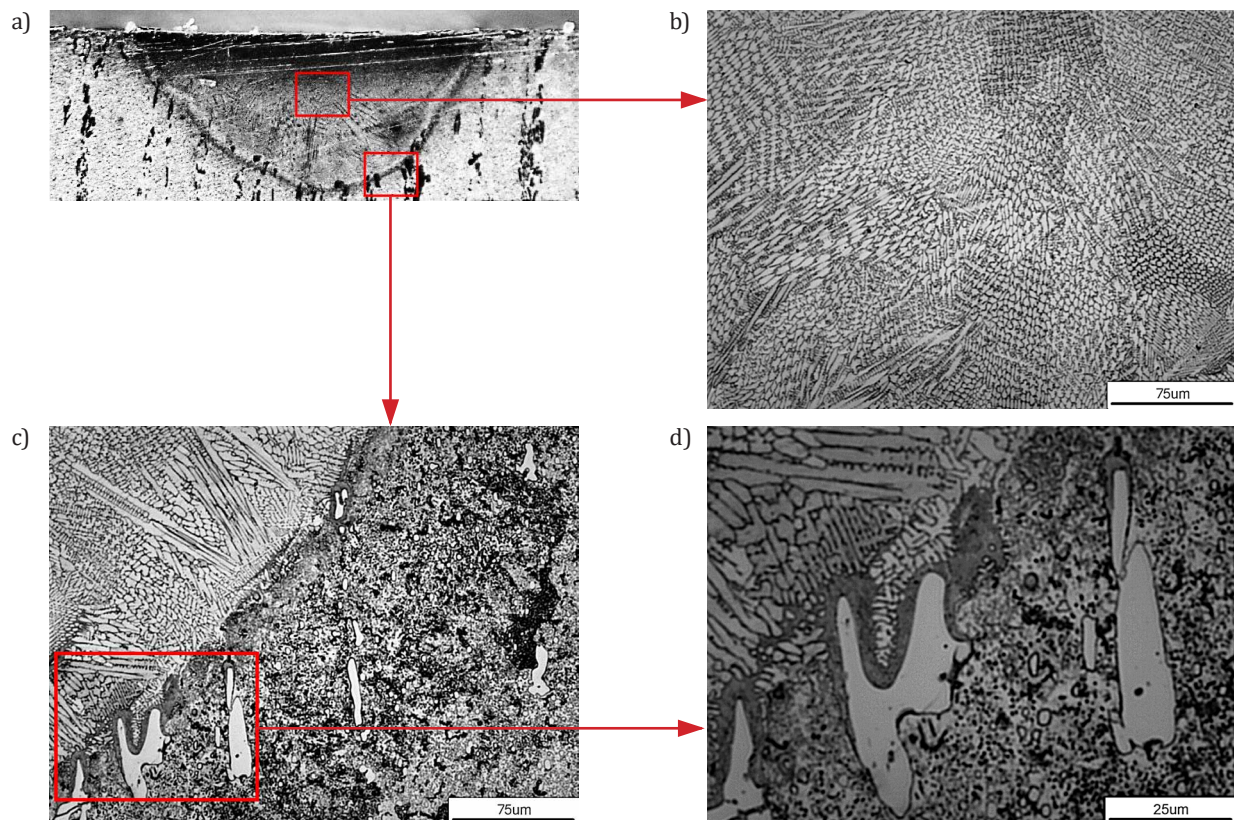
by the melted material. At constant beam power, the laser beam exposure time and, as a result, the amount of heat absorbed by the melting area, decreases as the scanning speed increases. It was noted that in the remelting area, a dendritic microstructure was obtained. In the border region where the NC11 steel parent material turns into the remelting area, large carbide precipitations were visible which dissolved in the course of remelting, along with the movement of the liquid metal pool.

In Figures 5–7, images of the macrostructure and microstructure of the remelting area and the heat affected zone (HAZ) on specimens of NC11 steel are shown, for different values of the speed of scanning with a laser beam.

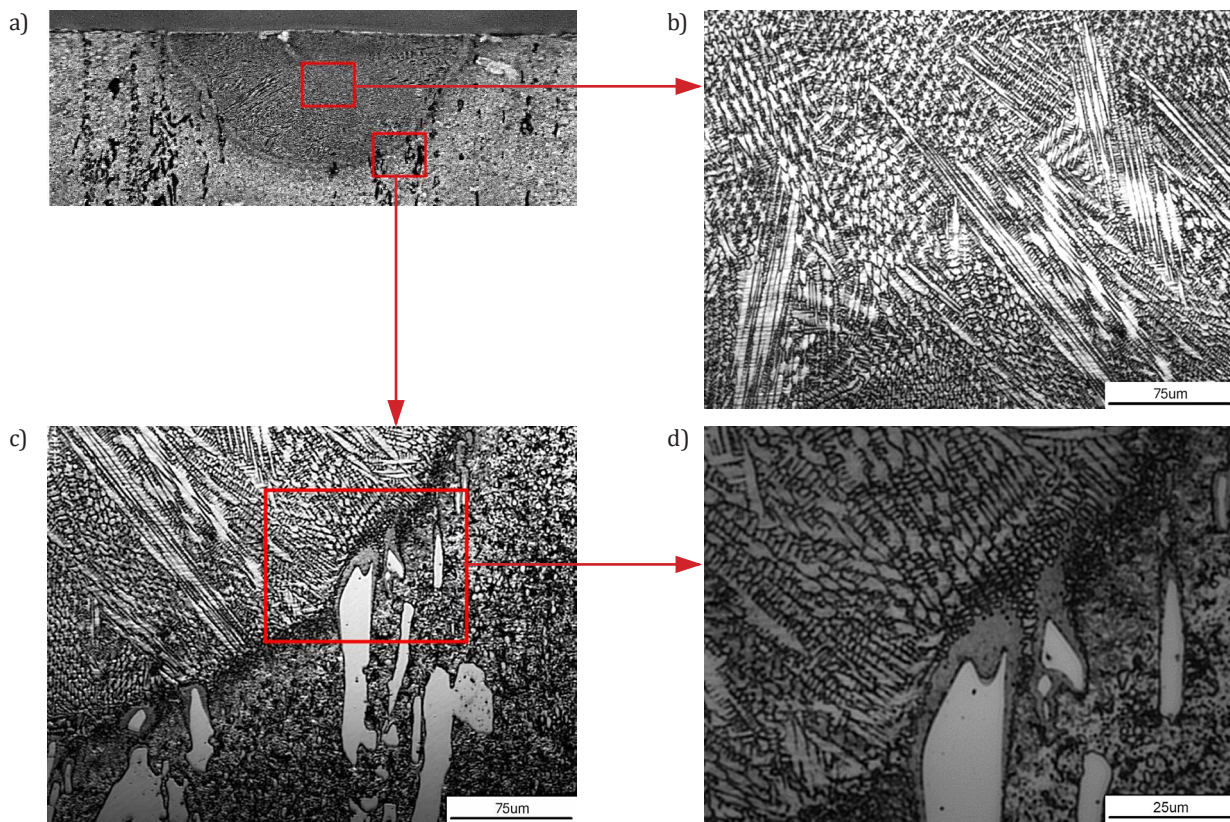
**Table 2**

Results of the remelting geometry and hardness measurements in the remelting area and in HAZ depending on the parameters of the laser-induced surface remelting process

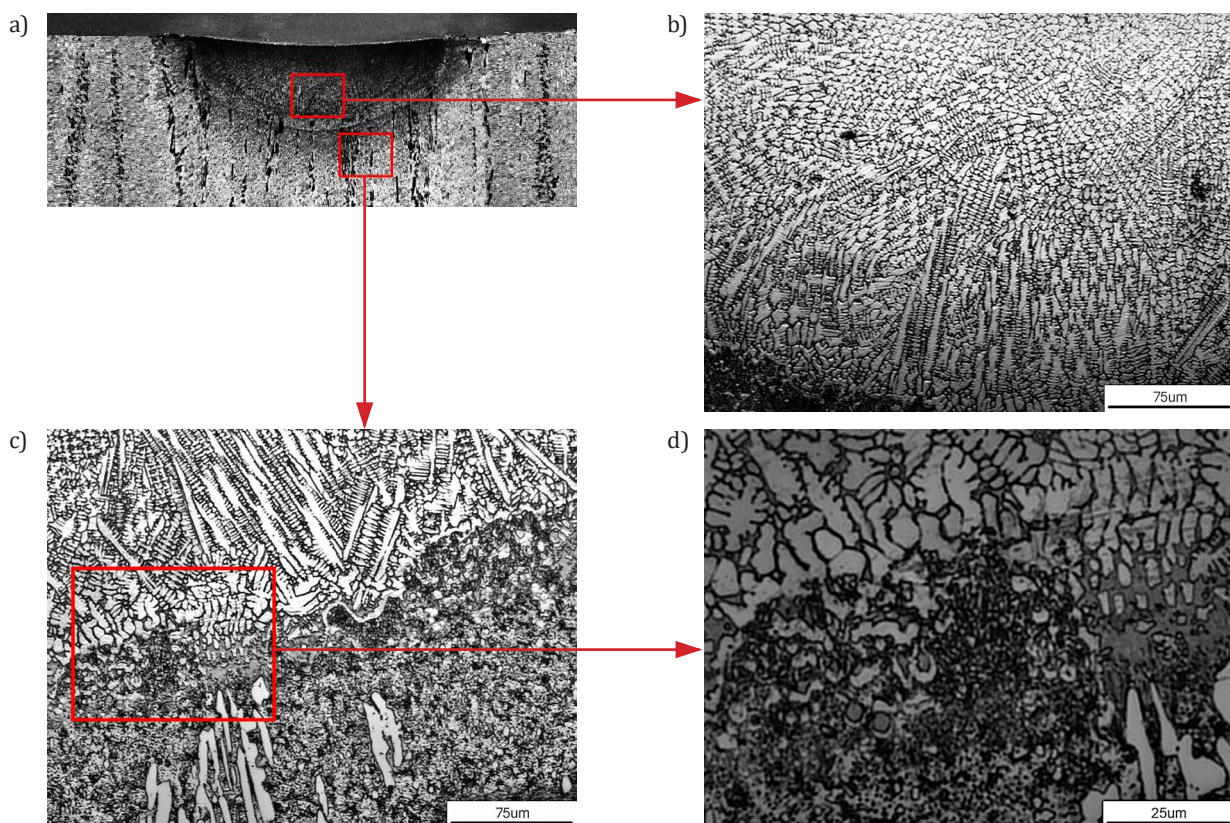
No.	Laser beam parameters		Remelting area geometry		Stress, MPa	HV <sub>0.3</sub> hardness average value in the area of:	
	Power, W	Scanning speed, v <sub>s</sub> , mm/s	Width, mm	Depth, mm		Remelting	HAZ
1	500	10	0.807	0.368	-403.9	505 ± 5	580 ± 6
2	500	20	0.761	0.290	-383.9	531 ± 6	615 ± 7
3	500	30	0.589	0.175	-348.5	552 ± 6	643 ± 7
4	Initial material				-138.6	250 ± 4	



**Fig. 5.** A view of the macrostructure and microstructure of NC11 steel remelted with the use of a laser beam operated at power  $P = 500$  W and scanning speed  $v_s = 10$  mm/s: a) macrostructure; b) remelting area; (c–d) HAZ



**Fig. 6.** A view of the macrostructure and microstructure of NC11 steel remelted with the use of laser beam operated at power  $P = 500$  W and scanning speed  $v_s = 20$  mm/s: a) macrostructure; b) remelting area; (c–d) HAZ



**Fig. 7.** A view of the macrostructure and microstructure of NC11 steel remelted with the use of laser beam operated at power  $P = 500$  W and scanning speed  $v_s = 30$  mm/s: a) macrostructure; b) remelting area; (c–d) HAZ



The measurements were taken with the use of the Vickers method under  $HV_{0.3}$  load. In each of the remelting areas, hardness was measured at least three times. A difference was observed between the hardness of the remelted metal regions and HAZ depending on the laser beam scanning speed. The highest hardness values of 580–643  $HV_{0.3}$  were observed in the heat-affected zone. In the remelted areas, hardness values ranged from 505 to 552  $HV_{0.3}$ . At the adopted parameters of the laser-based remelting process, approximately a 2- to 2.5-fold increase in hardness was observed compared to the initial state of the material. Local melting caused the dissolution of alloying elements and chromium carbides in the liquid metal pool. Rapid crystallization meant that the material in the molten area is homogeneous in the form of dendrites with high fragmentation of the precipitates, which promotes an increase in hardness compared to the native material.

The stress value measured on the remelted metal surface increased from 2.5 to 3 times compared to that found in the initial material. The material used for smelting is NC11 steel, which is delivered after plastic working under industrial conditions. Therefore, stresses were observed in the starting material (MR).

Stress measurements provide important information about the service properties of remelted areas as the state of stress is decisive for the nature and type of interaction between friction couples. Such a couple is created, on the one hand, of grains of the refractory material aggregate and, on the other, press mold linings in the course of the process of the fabrication of ceramic bricks (of e.g. fused alumina). Intensity of the abrasive wear process depends on the components of the load force and geometrical parameters characterizing grain shapes, the hardness of the abrasive material, and its state of stress [24–26].

### 3. SUMMARY AND CONCLUSIONS

As a result of the metallographic examination and hardness measurements performed, it can be concluded that in NC11 steel areas remelted with the use of a laser beam, a dendritic microstructure crystallizes with a hardness significantly higher than that of the parent material region. This is due to rapid crystallization which in turn results in its homogenization within the remelting area which favors the emergence of hard dendritic microstructure.

Based on observations made in the course of the performed research and the analysis of the obtained results, it can be concluded that that the laser-remelted areas of NC11 steel:

- are characterized with microstructure differing in a favorable way from that of the parent material,
- show different geometry (width and depth), hardness, and state of stress depending on the adopted parameters of the remelting process,
- show hardness which has increased relative to the parent material, with the maximum observed in the heat-affected zone.

The increased hardness of material in the HAZ compared to the remelted areas stems from the fact that in that very zone, partially unmelted large and very hard carbide precipitates remain, surrounded with hardening-induced structures.

Due to the hardness of the laser, surface hardening should be better than surface melting. However, during surface melting, the structure becomes homogeneous, which is more favorable during operation under wear conditions. The material containing various precipitates during wear promotes cracking and crumbling and pulling out of individual phases. The abrasive wear of a homogeneous material is steady. Therefore, despite the lower hardness of the melting area compared to the HAZ area, laser melting should be a better solution for extending the service life of elements made of NC11 steel.

The increase in hardness and stress values in the remelting area may be favorable to fostering the increased service life and durability of surfaces exposed to abrasive wear. Such a phenomenon occurs in the course of the interaction of aggregate grain edges on mold linings in the course of the press-molding of refractory material stampings.

The possibility of obtaining remeltings characterized with increased hardness on large surfaces of parts and tools made of NC11 steel can be considered as an alternative to the time-consuming and costly heat treatment processes currently applied to press mold components made of the alloy.

The application of the surface remelting process can also be considered a competitive solution to hard-facing with the use of expensive additives aimed at increasing resistance to abrasive wear. Padding welds of that type, in view of the existence of an excess weld metal, must be subject to further machining to obtain the required geometrical dimensions. In the case of laser-induced surface remelting, the face of the weld is flat and there is no excess weld metal since no filler is being added.

### Acknowledgements

*The study was carried out with the use of apparatus purchased using funds from the project 'Establishment of the Scientific and Research Inter-University Laboratory in Stalowa Wola', realized as part of the Operational Programme Eastern Poland 2007–2013, Priority axis I 'Modern Economy', Measure 1.3 'Supporting Innovativeness' as per contract No. POPW.01.03.00-18-016/12-00.*

### REFERENCES

- [1] Orłowicz A., Mróz M., Tupaj M., Kupiec B., Trytek A., Sondej K. & Kozak L. (2016). *A device for evaluation of scratch resistance of die inserts used to fabricate stampings of refractory materials*. 15 International Technical Systems Degradation Conference, Liptovský Mikuláš, 30 March – 2 April 2016, vol. 1, 70–73.
- [2] Orłowicz A., Mróz M., Tupaj M., Trytek A., Kupiec B., Korzeniowski M., Pająk D., Sondej K. & Kozak L. (2016). An assessment of appropriateness of the choice of parameters for refractory stampings fabrication process. *Archives of Foundry Engineering*, 16 (2), 55–60.

- [3] Orłowicz A., Mróz M., Tupaj M., Trytek A., Kupiec B., Korzeniowski M., Cisek Z., Sondej K. & Kozak L. (2006). Determination of unit pressure force in material volume in the course of refractory stamping press moulding. *Archives of Foundry Engineering*, 16 (2), 61–68.
- [4] Orłowicz A.W., Mróz M., Tupaj M., Trytek A., Kupiec B., Korzeniowski M., Sondej K. & Kozak L. (2016). The Effect of Carbides Orientation in NC11 Steel on Scratch Susceptibility of Die Inserts Used to Press Stampings for Refractory Shapes. *Archives of Foundry Engineering*, 16 (2), 95–98.
- [5] Orłowicz A., Mróz M., Tupaj M., Kupiec B., Kozak L. & Kij T. (2017). Application of ceramic coating to improve abrasive wear resistance of die inserts used to press-mould stampings of refractories. *Metallurgija*, 56 (3–4), 415–418.
- [6] Orłowicz A.W., Trytek A. & Malik J. (2013). *Formation of microstructure and service properties of cast iron castings by surface improvement with electric arc plasma*. Rzeszów: Oficyna Wydawnicza Politechniki Rzeszowskiej.
- [7] Orłowicz A.W., Tupaj M., Mróz M., Trytek A. & Betleja J.J. (2011). Kalorymetr przepływowy do pomiarów ciepłych w procesach spajania. Patent no. 211283, 16.11.2011.
- [8] Sondej K., Kozak L., Orłowicz A., Mróz M., Tupaj M., Trytek A., Kupiec B. (2016). A Mould insert with extended service life for press-moulding of stampings. Patent no. 16460035.5-1362, 02.06.2016.
- [9] Kim C.K., Lee S. & Jung J. (2006). Effects of heat treatment on wear resistance and fracture toughness of duo-cast materials composed of high-chromium white cast iron and low-chromium steel. *Metallurgical and Materials Transactions A*, 37, 633–643.
- [10] Chang K.K., Sunghak L. & Jae-Young J. (2006). Effects of Heat Treatment on Wear Resistance and Fracture Toughness of Duo-Cast Materials Composed of High Chromium White Cast Iron and Low-Chromium Steel. *Metallurgical and Materials Transactions A*, 37A, March, 633–643.
- [11] Pinedo C.E. & Monteiro W.A. (2001). Surface hardening by plasma nitriding on high chromium alloy steel. *Journal of Materials Science Letters*, 20, 147–149.
- [12] Larson J.A., Fischer R.B. (1982). Precipitation hardening chromium steel casting alloy U.S. Patent Apr. 27, 4,326,885.
- [13] Adetunji O.R., Musa A.A. & Afolalu S.A. (2015). Computational Modelling of Chromium Steel in High Temperature Applications. *International Journal of Innovation and Applied Studies*, 12 (4), 1015–1021.
- [14] Tillmann W., Schaak C., Hagen L., Mauer G. & Matthäus G. (2019). Internal Diameter Coating Processes for Bond Coat (HVOF) and Thermal Barrier Coating (APS) Systems. *Journal of Thermal Spray Technology*, 28 (1–2), 233–241.
- [15] Seshadri R.C. & Sampat S. (2019). Characteristics of Conventional and Cascaded Arc Plasma Spray-Deposited Ceramic Under Standard and High-Throughput Conditions. *Journal of Thermal Spray Technology*, 28 (4), 690–705.
- [16] Yingchun Xie, Chaoyue Chen, Marie-Pierre Planche, Sihao Deng, Renzhong Huang, Zhongming Ren & Hanlin Liao. (2019). Strengthened Peening Effect on Metallurgical Bonding Formation in Cold Spray Additive Manufacturing. *Journal of Thermal Spray Technology*, 28 (4), 769–779.
- [17] Aghasibeig M., Tarasi F., Lima R.S., Dolatabadi A. & Moreau C. (2019). A Review on Suspension Thermal Spray Patented Technology Evolution. *Journal of Thermal Spray Technology*, 28 (7), 1579–1605.
- [18] Nowotny S., Scharek S., Beyer E. & Richter K.H. (2007). Laser Beam Build-Up Welding: Precision in Repair, Surface Cladding, and Direct 3D Metal Deposition. *Journal of Thermal Spray Technology* 16 (3), 344–348.
- [19] Orłowicz A. & Mróz M. (2003). Microstructure and fatigue strength of A 356 alloy castings refined on the surface by rapid crystallization. *Zeitschrift für Metallkunde*, 94 (12), 1320–1326.
- [20] Orłowicz A. & Trytek A. (2003). Effect of rapid solidification on sliding wear of iron castings. *Wear*, 254, 154–163.
- [21] Orłowicz A. & Trytek A. (2003). A Susceptibility of iron castings to heat absorption from electric arc and to hardened-layer shaping. *Metallurgical and Materials Transactions*, 34A, 2973–2984.
- [22] Mróz M., Orłowicz A. & Tupaj M. (2013). Stress-rupture Tests of MAR-M-509 Cobalt Alloy Improved by Rapid Solidification. *Archives of Foundry Engineering*, 13 (1), 117–120.
- [23] PN-EN ISO 4957:2018-09 – Stale narzędziowe.
- [24] Hebda M. & Wachal A. (1980). *Trybologia*. Warszawa: WNT, internet edition by: Polskie Towarzystwo Trybologiczne 2005, <http://www.tribologia.eu/ptt/try/tr.htm>
- [25] Nastaj T. (2003). Badanie odporności na zużycie ścierne powłok napawanych stopami na bazie niklu. *Eksploatacja i Niezawodność*, 2, 49–51.
- [26] Pytko S. (1982). *Problemy wytrzymałości kontaktowej*. Warszawa: PAN.

# Connecting Castings for Operation under Conditions of Cyclic Temperature Changes

Andrzej Drotlew<sup>a</sup>, Bogdan Piekarski<sup>b\*</sup> 

<sup>a</sup>Przedsiębiorstwo Usług Odlewniczych POLCAST Sp. J., Piastów 19 Ave., 70-310 Szczecin, Poland

<sup>b</sup>West Pomeranian University of Technology in Szczecin, Department of Materials Technology, Piastów 19 Ave., 70-310 Szczecin, Poland

\*e-mail: [bogdan.piekarski@zut.edu.pl](mailto:bogdan.piekarski@zut.edu.pl)

© 2020 Authors. This is an open access publication, which can be used, distributed and reproduced in any medium according to the Creative Commons CC-BY 4.0 License requiring that the original work has been properly cited.

Received: 21 January 2020 / Accepted: 2 March 2020 / Published online: 30 March 2020  
This article is published with open access at AGH University of Science and Technology Press

---

## Abstract

The separable connections used in technological equipment of heat treatment furnaces (OTP) are described in this study. The equipment is used for the heat treatment of charges, i.e. for the thermal and thermo-chemical treatment of parts of machines and devices. OTP is used for the charge formation and its transport before, during and after heat treatment operations. Accessories of this type are usually compact structures composed of several or several dozen cast elements. The main components are grates and pillars, which form an outer contour of the OTP and also allow for the correct arrangement of heat-treated parts. To form a relatively rigid structure composed of the grates and pillars, it is necessary to join these components together. For this purpose, various types of separable connections are used, mainly of a cylindrical shape with threaded parts. The subject of this study is focused on the construction and operating conditions of typical OTP structures, as well as the methods of fastening the pillar in a grate, i.e. on the design of the bottom part of the pillar and the hole in the grate in which this pillar is embedded.

## Keywords:

castings for heat treatment plants, grates, pillars, thermal fatigue

---

## 1. INTRODUCTION

Separable connections allow for multiple connecting and disconnecting of structural elements without damaging them. They are often used to join cooperating elements included in the technological equipment of heat treatment furnaces (OTP) [1–4].

The use of these connections in OTP facilitates:

- replacement of those components that wear out faster during operation,
- changes in the internal design when required by changes in the type of charge (shape and size of heat-treated parts).

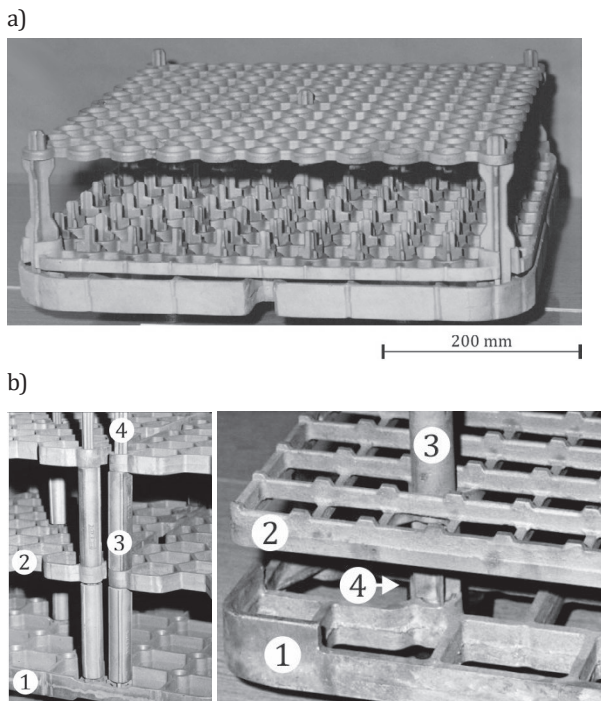
Loose fit allows parts of OTP for relatively free thermal deformation within the range of operating temperatures. However, it should be noted that the operating conditions of some types of OTP may also require the use of inseparable connections. This applies especially to OTPs which are operated on fully automated production lines [2].

Accessories of this type are structures usually composed of several dozen cast elements differing in shape and size.

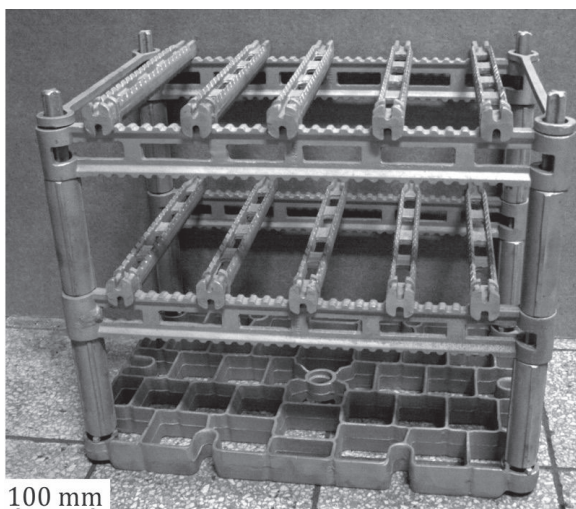
The main task of these structures is to form and handle the charge (heat-treated parts) during heat treatment operations. Castings are made from heat-resistant Cr-Ni or Ni-Cr steels, less often from nickel alloys. Thin walls of the same (as far as possible) thickness are a characteristic feature of individual OTP components (Figs. 1 and 2).

Typical examples of OTP commonly used in mass and large-lot heat treatment of small parts are the structures shown in Figures 1 and 2. They consist of a guide (load-bearing) grate, on which a structure composed of pillars and an intermediate grate (Fig. 1a), or pillars and crossbars (Figs. 1b and 2) rests. These accessories operate mainly in pusher furnaces, in which several units are simultaneously pushed in a row through the furnace working chamber. The number of levels in one OTP unit, where the heat-treated parts are laid or suspended, can be increased by means of the introduction of additional intermediate grates and spacers of the proper length (Fig. 1b).

The aim of this study was to describe separable connections on the example of a “hole-pillar” type connection joining the cooperating elements that form part of a typical OTP and to discuss the advantages and disadvantages of such designs.



**Fig. 1.** Single-level OTP for operation in the pusher furnace consisting of a guide grate, intermediate grates and pillars (a) and fragments of two multi-level OTPs for operation in the chamber furnace, the design of which also required the use of spacers (b): 1 – guide grate, 2 – intermediate grate, 3 – spacer, 4 – pillar; according to [2]

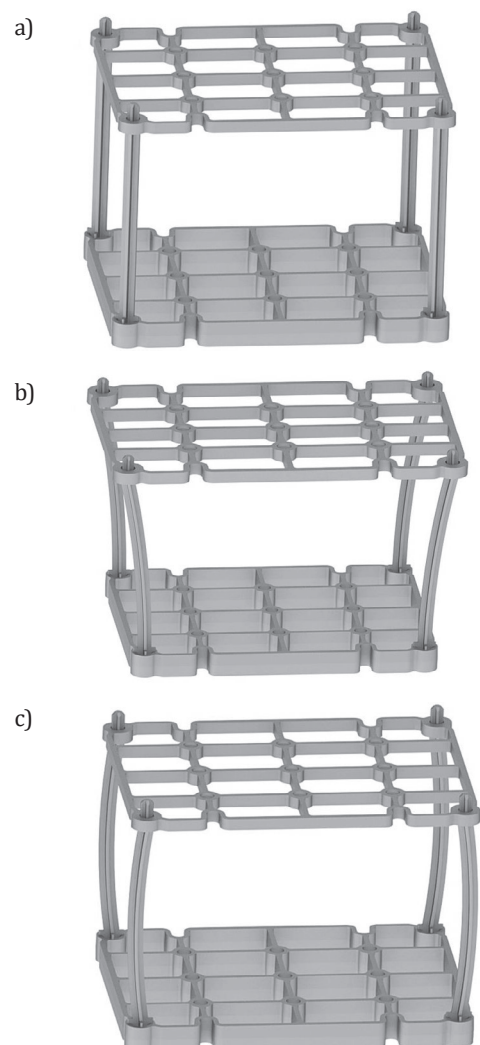


**Fig. 2.** Two-level OTP for operation in the pusher furnace consisting of a guide grate, pillars, spacers and crossbars [2]

## 2. OTP OPERATION

The initially satisfactory performance characteristics of OTP undergo degradation during operation due to the processes of aging, high temperature corrosion and thermal fatigue. As a result of the impact of these factors, deformation and/or cracking of the OTP walls takes place, combined with the detachment of fragments of these walls. At the same time, it should be assumed that resistance to thermal fatigue is the main factor responsible for the durability of OTP [2, 5–6].

Changes in the dimensions of OTP components during heating/cooling of the charge subjected to heat treatment or thermo-chemical treatment are of a complex nature resulting from the synergy of numerous factors, such as maximum operating temperature, type of treatment, conditions of the charge cooling and its mass, the shape and dimensions of heat-treated parts, or the degree of the OTP structure complexity (see Figs. 1 and 2). The simplest design of the equipment is shown in Figure 3a. Connecting the grates with pillars reduces the mutual risk of thermal deformations occurring in parts of the guide grate and intermediate grate. In each cycle of the heat treatment, in the intermediate grate with the walls usually thinner than the walls of the guide grate, the process of heating and cooling proceeds at a much higher speed. Therefore, pillars connecting the grates are bent outwards during heating of the charge (Fig. 3b) and inwards during cooling (Fig. 3c). The cyclic nature of these processes means that in the OTP whose design is based on a guide grate and intermediate grates (Fig. 3a), mainly pillars (Fig. 4) and corners of the grates will be damaged [2].



**Fig. 3.** Diagram of changes in the shape of OTP during operation: a) condition before operation; b) high-speed heating; c) fast cooling; according to [7]

Industrial practice also shows that in this type of OTP, pillars are the components which are exposed to the highest wear rate [2]. Their decommissioning occurs primarily as a result of the through-cracking (breaking off) of the lower part of the pillar mounted in a hole made in the guide grate (Fig. 4).

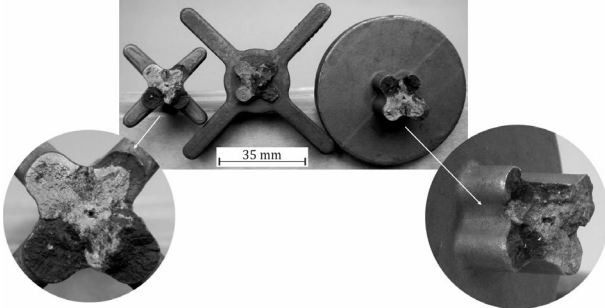


Fig. 4. Fractures in the lower part of the pillar formed as a result of the breaking off of its fragment during operation

3. SEPARABLE CONNECTIONS OF THE "HOLE-PILLAR" TYPE

Pillars serving as vertical supports in the OTP structure are the main component which connects the guide grate

and intermediate grates. Traditionally designed (Figs. 5 and 6), they have a fixed, cruciform cross-section that provides them with the expected stiffness, a length from 200 to even 3000 mm, and cross-sectional dimensions described by a circle with a diameter of 15 to 50 mm.

The pillars consist of three main parts (Figs. 1-3):

- shaft – a long part whose basic task is to enable the installation of other transverse elements of the OTP structure in the guide grate. The length of the shaft depends on the shape and dimensions of heat-treated parts and on their arrangement; it is also limited by the height of the furnace working chamber,
- support – forming the abutment surface necessary for mounting the pillar. As a rule, it has a 4-arm or round shape (Fig. 4). The support has a thickness of the shaft wall and a diameter corresponding to the outer diameter of the hole in which the pillar is mounted,
- base – a short part, used to fix the pillar in the guide grate. Its length is usually equal to the height of the guide grate.

The thin-walled structure of the OTP cast components results in their simultaneous solidification. Therefore, it is inevitable that larger volumes of the cast material separated by the thin walls will form areas with an increased concentration of internal shrinkage defects, such as shrinkage porosities and cavities.

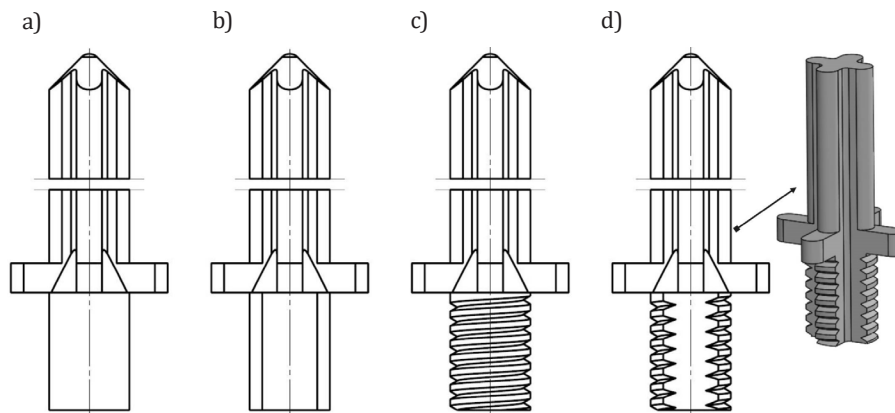


Fig. 5. The design of the pillar with a cylindrical base (a); cylindrical-oval base (b) and additionally threaded base (c, d)

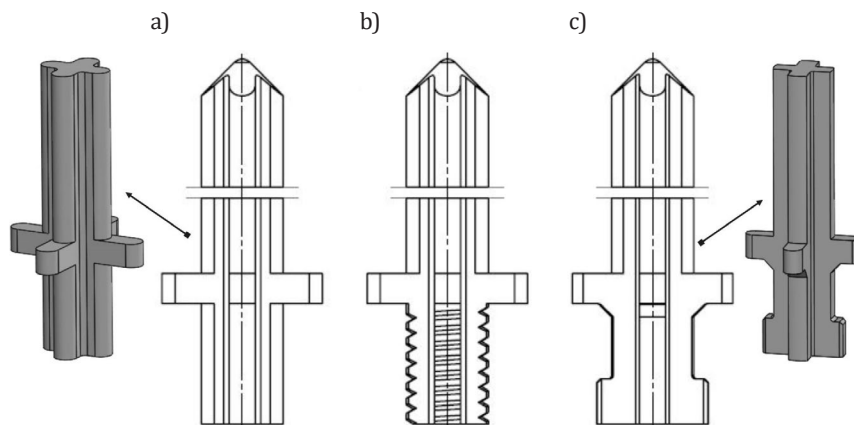


Fig. 6. The design of the pillar with a cruciform cross-section base. Base: a) standard; b) with extra threads; c) bayonet-like shaped

In a pillar, such a massive area (local thermal node) that will solidify longer than the neighboring areas is the common area of the shaft and support (see Fig. 4). In pillars of the design shown in Figure 5, the occurrence of shrinkage defects can be significantly minimized by feeding an extra volume of liquid metal to this area through the base of the pillar during the solidification period. The design of a gating system with a lateral feeder (riser) ensuring liquid metal flow to the mould cavity from the side of the pillar base seems to be a solution whose effectiveness is guaranteed by a sufficiently large cross-section of the pillar base. In other pillars (Fig. 6), this solution will not be effective due to the small cross-section of the pillar base.

In all pillars (Figs. 5 and 6), the casting of the base does not require the use of cores. If the roughness of the raw surface is  $R_a < 40 \mu\text{m}$ , the pillars can be easily and efficiently fixed in the holes of the guide grate without the need for mechanical treatment. On the other hand, it is necessary to ensure that both the base surface and other surfaces of these castings are free from defects typically occurring in the as-cast condition, such as microfolds or micro-cold shuts. Defects of this type can facilitate the nucleation and development of cracks and accelerate in this way the

destruction of pillars under the conditions of thermal fatigue.

The shape of the holes made in the guide grate for fixing the pillars is shown in Figure 7.

In the design of the holes, there are also areas (local thermal nodes) with increased concentrations of internal defects. These are the places in the grate walls that are directly adjacent to the holes. Their massiveness can be reduced by properly selected radii [1–3] and recesses made in the material surrounding the hole (Fig. 7a).

Generally, the outer contour of the grate undergoes faster degradation during operation than the inner part because it is heated/cooled at a higher speed compared to the middle part where the charge is resting. At the same time, the places in the walls adjacent to the holes are the source of the largest number of cracks [2]. This degradation process can be slowed down by the use of reinforcing ribs (Fig. 8), similar to shrinkage ribs used in casting. They facilitate heat dissipation from the wall sections with the largest thickness but also make the grate structure more rigid. Therefore, the decision to introduce them should be carefully considered, taking into account the variable thermal loads to the effect of which the OTP is subjected during its operation.

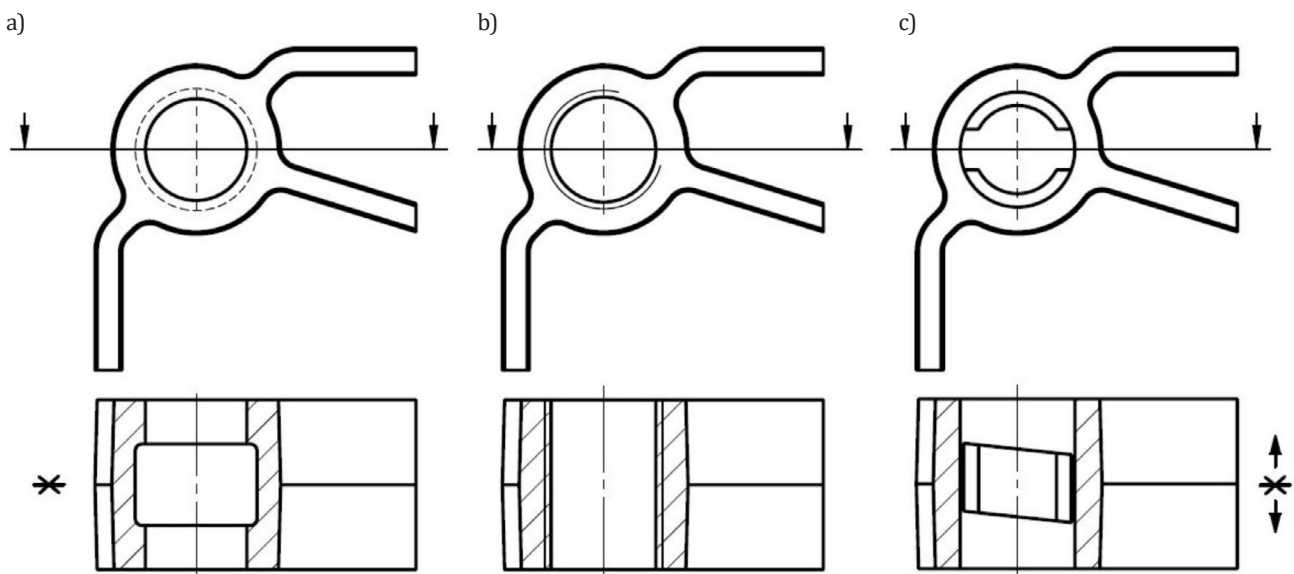


Fig. 7. The design of the holes in the guide grate for fixing the pillars shown in Figures: a) 5a-b and 6a; b) 5c-d and 6b; c) 6c

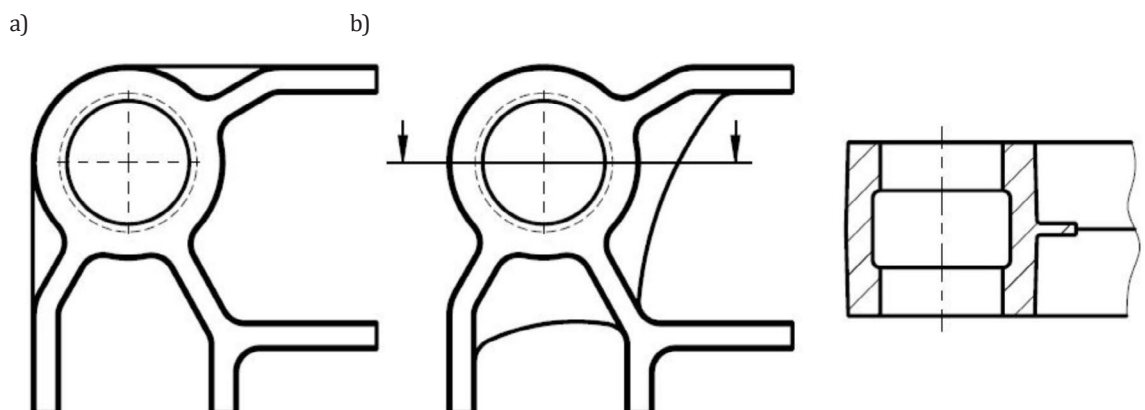


Fig. 8. Reinforcing ribs in the corners of the grate with holes for fixing the pillars: a) external; b) internal

The thickness of the ribs  $g$  is calculated following the design recommendations for shrinkage ribs [8, 9], based on the casting wall thickness  $d$ :  $g = (0.2-0.3) d$ , where the minimum value of  $g$  should be  $\geq 2.5$  mm.

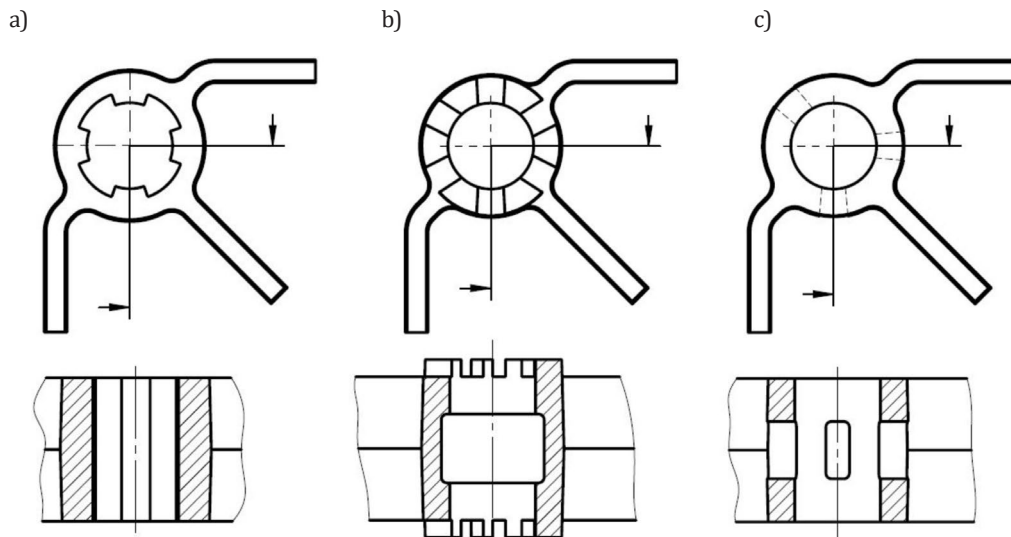
Temperature gradients in more massive areas of the OTP can also be reduced by recesses made in the material adjacent to the holes (Fig. 9). They facilitate the circulation of the cooling liquid (coolant) around the "hole-pillar" surface, thus allowing for more intense cooling.

The first two solutions require additional comments and explanations (Fig. 9a and b). In the inner holes, threaded ribs can also be used (Fig. 9a). In the holes with recesses on the front surfaces (Fig. 9b), pillars with round support should be mounted (see Fig. 4).

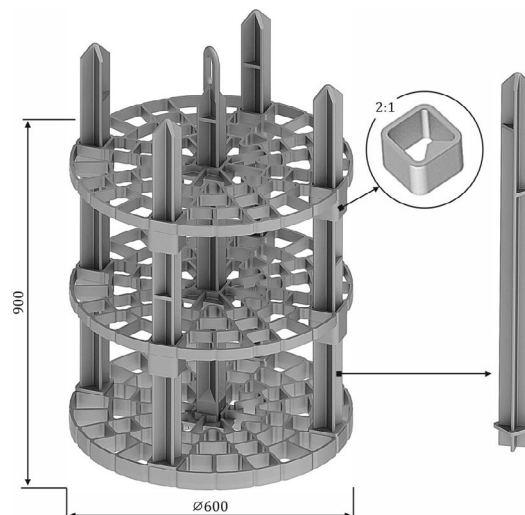
Apart from the typical, previously described designs, separable connections of the "hole-pillar" type can also have another non-standard form (see Fig. 10). In the method of fixing intermediate grates in OTP shown in the drawing, it is not only important that this method solves the problem of positioning the grates in a completely different

manner, but it is also important that the consequence of this change will be an OTP with a lighter weight due to the elimination of spacers and metal volumes in those areas that would be considered very massive (increasing instantaneous temperature gradients), if a traditional solution were used. As a result of this modification, one can expect both a reduction in the OTP operating cost and an increase in its durability.

Multi-level OTP designs consist of the corresponding number of intermediate grates / crossbars and spacers of the proper length (Figs. 1b, 2 and 10). Solutions are also used in which the height of the first and, at the same time, lowest level can be set by a pillar with two-step cross-section (see Fig. 1b, right). In the OTP shown in Figure 10, the design problem has been solved in a different way. The unit can have maximum 4 levels. Their height is determined by proper spacing of the horizontal ribs along the pillar height (see Fig. 10), where a rib is placed on the pillar at the next level but rotated in a horizontal plane by  $90^\circ$  in relation to the previous one.



**Fig. 9.** The solutions used in the design of grate holes for fixing the pillars: a) internally ribbed hole; b) hole with recesses on the front surfaces; c) hole with recesses on the side surface



**Fig. 10.** OTP for operation in the pit furnace with pillars and holes for fixing these pillars of a non-typical design

A retainer rests on the rib and supports the intermediate grate. In this OTP, the idea of using traditional (round) holes for fastening pillars was abandoned. They were replaced with square holes blocking the pillars rotating movement and facilitating the OTP assembly.

#### 4. FINAL REMARKS

To have an unrestrained possibility of introducing changes to the dimensions of individual OTP components, it is necessary to understand the processes which a structure of this type will be exposed to during operation. Generally speaking, referring to earlier comments on the design of separable "hole-pillar" type connections, the following should be stated:

1. Use connections where the coolant can penetrate relatively easily between the pillar shaft and the mounting hole. This will be beneficial for OTP durability as it will reduce the stress concentration in these areas of the structure. This condition is better met by pillars with a cruciform cross-sectional base than those with a cylindrical oval base.
2. Avoid rigid connections. These are primarily the threaded connections, which in practice prevent individual OTP elements from relatively free changes of dimensions in the variable field of temperatures. Regardless of this fact, their use in large and high OTPs is usually necessary. When OTP is moving inside the furnace chamber or outside the furnace, there is always a risk that the charge will get "loose" and the heat-treated parts will fall off the hooks.

3. When designing OTP elements, all solutions that allow the reduction in the volume of local thermal nodes should be used, remembering that the nodes:
  - give rise to the concentration of thermal stresses in these areas during casting manufacture and later operation,
  - give rise to the concentration of internal shrinkage defects, which are convenient places for later nucleation and development of cracks.

#### REFERENCES

- [1] Steinkusch W. (1985). Verbesserte Werkstoff und Konstruktionen verringern Betriebskosten bei der Wärmebehandlung. *Fachberichte Hütten. Metall.* 23, 746–749.
- [2] Piekarski B. (2012). *Odlewy ze stopów żarowytrzymałych w piecach do obróbki cieplnej*. Szczecin: Wydawnictwo Uczelniane ZUT w Szczecinie.
- [3] Folders: Lohmann, Cronite, Pose-Marre, Technoalloy, MA-NOIR PETRO-CHEM, AFE Technologies, NCK.
- [4] Drotlew A., Piekarski B. & Słowik J. (2017). The design of cast technological equipment for heat treatment furnaces. *Archives of Foundry Engineering*, 17(3), 31–36.
- [5] Bajwoluk A. & Gutowski P. (2017). The Effect of Cooling Agent on Stress and Deformation of Charge-loaded Cast Pallets. *Archives of Foundry Engineering*, 17(4), 13–18.
- [6] Bajwoluk A. & Gutowski P. (2019). Stress and crack propagation in the surface layer of carburized stable austenitic alloys during cooling. *Materials at High Temperatures*, 36(1), 9–18.
- [7] Piekarski B. (2010). Damage of heat-resistant castings in a carburizing furnace. *Engineering Failure Analysis*, 17(1), 143–149.
- [8] Kniagin G. (1977). *Metalurgia i odlewnictwo staliwa*. Katowice: Wydawnictwo „Śląsk”.
- [9] Telejko I. (1986). *Naprężenia i pęknięcia w odlewach staliwnych*. In: *Zarys metalurgii i odlewnictwa staliwa: praca zbiorowa. Cz. 2, Odlewnictwo*, Ed. A. Staronka, Skrypty Uczelniane Akademia Górniczo-Hutnicza nr 1023, 180–224.